INSULIN REGULATES NEURO-VASCULAR COUPLING THROUGH ASTROCYTES

Ana Fernandez[1,2], Laura Martinez-Rachadell[1,2], Jonathan Zaguirre-Valdivia[1,2,3], Marta Navarrete[1], Victor Munive[1,2], Jose Carlos Davila[2,4], Jaime Pignatelli[1,2], Santiago Guerra-Cantera[1,2], Emilia Viedma-Moreno[1,2], Sonia Diaz-Pacheco[1], Maria L. de Ceballos[1], Rocio Palenzuela[5], Samuel Ruiz de Martin Esteban[5], Ricardo Mostany[6], Julia Pose[2,7], Cristina Garcia-Caceres[8], Matthias Tschöp[8], Teresa Iglesias[2,7], Antonia Gutierrez[2,4], and Ignacio Torres Aleman[2,3,9]

[1]Cajal Institute, CSIC, Madrid, Spain; [2]Ciberned, Spain; [3]Achucarro Basque Center for Neuroscience, Leioa, [4]Dept. Cell Biology, Genetics and Physiology, Instituto de Investigación Biomédica de Malaga-IBIMA, Faculty of Sciences, University of Malaga, Spain; [5]Faculty of Experimental Sciences, Universidad Francisco de Vitoria; Madrid, Spain; [6]Neuroscience Program, Tulane University School of Science and Engineering, New Orleans, USA. [7]Institute of Biomedicine, CSIC, Madrid, Spain, [8]Institute for Diabetes and Obesity, Munich, Germany, and [9]Ikerbasque Basque Science Foundation, Bilbao. Spain.

Abstract

Circulating insulin enters the brain through mechanisms incompletely characterized. We now report that mice lacking insulin receptors (IR) in astrocytes (GFAP-IR KO mice) show blunted brain responses to insulin, uncoupling of brain blood flow with glucose uptake with concomitant changes in brain vasculature and glucose transporter 1 levels. IR-deficient astrocytes show increased expression of HIF-1α/VEGF, promote growth of co-cultured endothelial cells, display increased reactive oxidant species (ROS) and disturbed mitochondrial activity. Treatment with the antioxidant N-acetylcysteine (NAC), ameliorated high ROS levels, normalized angiogenic signaling, and mitochondrial function including mitochondrial glucose and oxygen sensors. In vivo treatment with NAC also normalized brain perfusion. Thus, insulin receptors in astrocytes regulate neuro-vascular coupling.

Introduction

Recent observations indicate that circulating insulin enters the brain parenchyma through a transport mechanism involving its receptor in brain endothelial cells (Gray et al., 2017), although more recent observations indicate that the process may be IR independent (Hersom et al., 2018; Rhea et al., 2018). Astrocytes seal brain endothelial cells of brain capillaries by wrapping them with their end-feet (Mathiisen et al., 2010). In this way, astrocytes constitute an additional cell layer of the blood-brain-barrier (BBB) (Zlokovic, 2008). Once insulin has being transported across endothelial cells (King and Johnson, 1985), it may be taken up by astrocytes either to be further transported into the brain parenchyma through transcytosis (Simionescu et al., 2002), to modulate the activity of these glial cells (Cai et al., 2018; Garcia-Caceres et al., 2016), or both.

Insulin is not only a major regulator of body energy handling, but also exerts many other functions, including vasoactive effects (Warmke et al., 2021; Zheng and Liu, 2015), that may modulate brain perfusion (Novak et al., 2014). Indeed, endothelial dysfunction is associated to insulin resistance (Muniyappa and Sowers, 2013), and is reflected in reduced cerebral perfusion (Rusinek et al., 2015), leading to suboptimal oxygen levels in the brain. In this organ, astrocytes sense changes in oxygen pressure (PO_2), providing feedback information to processes involved in cerebral perfusion (Angelova et al., 2015), through mechanism under intense scrutiny (Marina et al., 2018). Astrocytes, together with other cellular components of the BBB are involved in neurovascular responses to changes in brain activity (Iadecola, 2017). Because brain metabolic demands and blood flow are coupled through functional hyperemia (Roy and Sherrington, 1890), astrocytes, that are sensitive to insulin, have been proposed to participate both in glucose and O_2 sensing (Marina *et al.*, 2018).

We recently showed that insulin receptors in astrocytes participate in brain glucose handling (Fernandez et al., 2017; Garcia-Caceres *et al.*, 2016; Hernandez-Garzon et al., 2016). Astrocytes have an intricate relationship with brain vessels through specialized cytoplasmic extensions termed end-feet (Kacem et al., 1998), placing them at the crossroad between metabolic and vasoactive signals. Indeed, PO_2 modulates vessel formation in conjunction with metabolism (Fraisl et al., 2009). Ultimately, the size of the brain vascular tree will affect the level of perfusion to this organ. Because changes in brain perfusion and metabolism are associated to aging (Toth et al., 2017), are exacerbated in parallel in different brain pathologies (Iadecola, 2017), and probably herald development of Alzheimer´s disease (Iturria-Medina et al., 2016; Ruitenberg et al., 2005), we examined the role of insulin receptors (IR) in astrocytes in brain perfusion, as insulin resistance is associated to aging and neurodegeneration.

To help clarify the route of entrance of circulating insulin into the brain, we analyzed its brain uptake in mice lacking IR in astrocytes. Ablation of IR in astrocytes blocked entrance of, and brain responses to, circulating insulin, suggesting that astrocytes form part of the intracellular pathway of passage of this hormone into the brain. In vivo and in vitro analysis of the role of astrocytic IR in brain function also revealed that glucose uptake and brain perfusion are integrated by astrocytic IR. This receptor is essential to maintain normal mitochondrial function in astrocytes and brain vasculature.

Results

IR are present in glial end-feet.

We first determined whether IR are present in astrocytic end-feet ensheathing endothelial cells of the BBB, as its presence in this compartment will allow circulating insulin to readily access astrocytes. Using combined IR immunogold labeling and

electron microscopy we localized these receptors in astrocytic end-feet (Figure 1A,B). This anatomical location, in close proximity to endothelial cells, together with the expression of IR in the latter type of cells (Figure 1B), or as an yet uncharacterized transporter (Rhea *et al.*, 2018), would allow the passage of circulating insulin into astrocytes by transcytosis through endothelial cells (Gray *et al.*, 2017).

Astrocytic IRs are involved in brain IR activation and stimulation of astrocyte signaling by circulating insulin.

As already documented (Sartorius et al., 2015), systemic administration of insulin results in significant activation of brain IR (*$p<0.05$ vs saline, t-test; Figure 2A). However, GFAP IR KO mice show attenuated responses to peripheral insulin injection, as determined by significantly reduced phosphorylation of brain (*$p<0.05$ vs littermate controls, t-test; Figure 2B), but not muscle IR (Figure 2C). The reduction in brain IR phosphorylation was not related to lower brain IR levels in mutant mice due to the ablation of astrocytic IR (**$p<0.01$ vs control littermates, t-test; Suppl Figure 1A), since receptor activation was normalized by its relative levels (similar between tamoxifen-treated and non-treated mice; see lower blot in Figure 2B). Conversely, direct intra-parenchymal insulin injection into the brain of GFAP IR KO mice resulted in IR activation similar to littermate controls (Suppl Fig 1B). Furthermore, GFAP IR KO mice show normal brain insulin-like growth factor I (IGF-I) receptor phosphorylation in response to systemic injection of this close relative of insulin (Suppl Fig 1C), indicating specific loss of brain sensitivity to systemic insulin.

Since changes in intracellular Ca^{2+} levels are used as a proxy of astrocyte activity (Ma et al., 2016), we next determined whether circulating insulin modulates intracellular Ca^{2+} in astrocytes of GFAP IR KO mice. We monitored in vivo Ca^{2+} levels in astrocytes located in the somatosensory cortex by two-photon laser-scanning fluorescence microscopy using a genetically-encoded Ca^{2+} indicator (Lck-GCaMP6f) (Figure 3A,B). We found that systemic administration of insulin (3 IU/kg) elicited increases in Ca^{2+} spikes frequency in control littermates but not in GFAP IR KO mice (**$p<0.01$, Kruskal-Wallis followed by Wilconxon test; Figure 3C-D), confirming that astrocytic IRs are necessary for astrocytes to respond to systemic insulin.

Astrocytic IRs are involved in brain uptake of circulating insulin.

To trace cellular pathways involved in the passage of circulating insulin into the brain, we injected mice with digoxigenin-labelled insulin (Dig-Ins) in the carotid artery and examined its route of entrance by double immunolabelling with anti-Dig and cell-specific markers. In GFAP IR KO mice injected with vehicle (oil), neuronal digoxigenin staining was readily seen (Figure 4A, panels b-c, and B). However, in tamoxifen-treated GFAP IR KO mice, neuronal staining was lost (Figure 4C, panels b-c, and D). In addition, a strong Dig-Ins staining in vessels was seen in these animals (Figure 4C, panel a, and Suppl Fig 1D), suggesting that in the absence of astrocytic IR, Dig-Ins is retained inside the endothelium without crossing into the brain parenchyma.

Brain insulin resistance uncouples brain flow and glucose uptake.

Because young GFAP-IR KO mice have reduced brain glucose uptake, probably related to decreased glucose transporter 1 levels (GluT1) in the brain (Garcia-Caceres *et al.*, 2016) (Suppl Figure 1E), we determined brain perfusion, as blood flow and glucose uptake may be linked through astrocytes (Koehler et al., 2009), and insulin affects endothelial function (Warmke *et al.*, 2021; Zheng and Liu, 2015). Moreover, reduced GluT1 elicits compensatory increases of the angiogenic factor VEGF (Jais et al., 2016)

that can promote vessel growth. Indeed, disturbed brain perfusion and glucose uptake go hand-on-hand in different brain pathologies.

We examined brain perfusion using single-photon emission computed tomography (SPECT) of ^{99}Tc-HMPAO (Apostolova et al., 2012). Young (~3 months of age) GFAP-IR KO mice present significantly increased brain perfusion, while at later ages (>1 year old mice) brain perfusion significantly decreased (**p<0.01 vs littermates, t-test; Figure 5A). Perfusion was altered along age only in GFAP-IR KO mice ((**p<0.01 vs littermates, t-test; Suppl Figure 2A,B), and depended on the timing of IR deletion since when tamoxifen was given to old GFAP-IR KO mice, no alterations were seen (Suppl Fig 2C). Changes were specific for astrocytic IR as mice lacking astrocytic IGF-I receptors did not show altered brain perfusion (Suppl Figure 3A).

Changes in redox status may interfere with cellular uptake of ^{99}Tc-HMPAO (Jacquier-Sarlin et al., 1996). Because astrocytes lacking IR show changes in mitochondrial function compatible with increased generation of oxidative radicals (Garcia-Caceres *et al.*, 2016), and astrocytes are the predominant cell type accumulating ^{99}Tc-HMPAO in brain (Zerarka et al., 2001), we determined levels of reactive oxygen species (ROS) in the brain of GFAP-IR KO mice. Not significant increases were seen in brain ROS levels in young mice, whereas adult GFAP-IR KO mice show slightly decreased ROS levels as compared with vehicle-injected controls (Suppl Figure 3B). Since increased ROS interferes with ^{99}Tc-HMPAO uptake (Maulucci et al., 2016b), changes in ^{99}Tc-HMPAO uptake do not seem related to ROS levels as they change in the same direction.

Previously, we reported that GFAP-IR KO mice show reduced brain glucose uptake at young age (Garcia-Caceres *et al.*, 2016). Indeed, ^{18}FDG-PET analysis confirmed decreased brain glucose uptake in young GFAP-IR KO mice (***p<0.001, t-test; Figure 5B). However, in older GFAP-IR KO mice, brain glucose uptake was slightly increased as compared to control, vehicle-injected mice (Figure 5B). Brain glucose uptake was significantly changed along age only in GFAP R KO mice, as their control littermates did not show significant changes along time (Suppl Fig 2D,E). Collectively, these observations suggest that GFAP-IR KO mice have uncoupled brain blood flow and brain glucose uptake with a changing pattern along time.

Astrocytic IR modulates brain angiogenesis.

Since brain ^{99}Tc-HMPAO uptake is mostly reflecting astrocyte accumulation and changes in astrocyte metabolism may interfere with it (Zerarka *et al.*, 2001), we determined several vessel biomarkers to confirm that the observed changes are related to brain vascularity. Levels of von Wilebrand factor (vWF), a marker of microvessel density (Thomas et al., 2015), were increased in young, but not in adult GFAP-IR KO mice (*p<0.05, t-test; Figure 6A), matching the observed age-dependent changes in perfusion (Figure 5A). Further, morphological evaluation of brain vessels in GFAP-IR KO mice confirmed increased vascularity in young but not older GFAP-IR KO mice (**p<0.01, t-test; Figure 6B). Increased vascular density was already present in adult control mice compared to younger ones (Figure 6B, lower and upper histograms), in agreement with increased perfusion values (Figure 5A, lower and upper histograms). Accordingly, brain mRNA levels of Sirt1, a marker of angiogenesis (Das et al., 2018), were increased in young GFAP-IR KO mice (**p<0.01, t-test; Figure 6C). However, the myelin associated glycoprotein (MAG)/proteolipid protein 1 (PLP1) ratio, a marker of white matter perfusion (Barker et al., 2014), remained unchanged in young mice (Suppl Fig 3C), suggesting that gray matter perfusion is specifically affected.

GFAP-IR KO mice showed also time-dependent changes in brain levels of the HIF1a/VEGF angiogenic pathway, with increased expression in young mice and slightly reduced or normal in older mice (*p<0.05, and ***p<0.001 vs controls, t-test; Figure 7A,B). Furthermore, mRNA expression of angiogenic proteins such as TGFβ3, VEGFa/c, and Errb2, was increased in young mice (*p<0.05, **p<0.01 and ***p<0.001, t-test; Figure 7C), as determined by qPCR, whereas at later ages expression of these genes were either reduced or within control levels (*p<0.05, t-test; Figure 7D). Other genes related to angiogenesis such as Mmp14 and PTGS1 remained unaffected in both young (Suppl Fig 3D,E), and older GFAP-IR KO mice (not shown). Further, expression of these angiogenic markers, including Mmp14 and PTGS1, was increased in the brain of young mice lacking IR in tamoxifen-regulated GLAST-astrocytes (GLAST-IR KO mice), that show a larger downregulation of IR in astrocytes (Garcia-Caceres *et al.*, 2016) (*p<0.05, **p<0.01 and ***p<0.001, t-test; Suppl Fig 4). This confirms increased expression of angiogenic markers in brain of young mice lacking IR in either GFAP or GLAST astrocytes.

IR modulates angiogenic signaling by astrocytes.

As mice lacking IR in astrocytes show changes in brain levels of several angiogenic mediators, we determined whether astrocytes are directly related to these changes. Reduced IR in astrocytes was obtained by either RNA interference or by culturing astrocytes from GFAP-IR KO mice. After reducing IR expression in astrocytes by RNA interference (sh-IR), levels of the angiogenic signals HIF1α and VEGF increased (**p<0.01, t-test; Figure 8A,B). This is accompanied by increased expression of VEGFa and $TGF\beta_3$ (*p<0.5 and **p<0.01, t-test; Figure 8C), while other angiogenic signals, including VEGFc, PTGS1, MmP14, Errb2 and vWF remained unaltered (not shown). Thus, several, but not all the angionenic-related molecules altered in brain were also altered in IR-deficient astrocytes. Conversely, insulin upregulates this pathway in wild type astrocytes (**p<0.01, t-test; Suppl Fig 5A), which reveals a complex, biphasic angiogenic response of astrocytes to insulin signaling.

Because reduced astrocytic IR function affects neuronal activity (Garcia-Caceres *et al.*, 2016), we determined whether its reduction also impacts on brain endothelial cells, as astrocytes are in close contact with them and their growth and differentiation may be modulated by astrocyte-derived angiogenic signals (Cohen-Salmon et al., 2021). For these experiments we used astrocytes obtained from GFAP IR KO mice with reduced IR levels (**p<0.01, t-test; Suppl Fig 5B) and co-cultured them with wild type endothelial cells. We observed that higher levels of angiogenic markers in co-cultures of astrocytes lacking IR (HIF1α and VEGF, **p<0.01, t-test; Figure 8D,E), were accompanied by endothelial growth, as determined by increased levels of CD31, a marker of endothelial cells (***p<0.01, t-test; Figure 8F) or markedly stronger CD31 immunostaining of wild type endothelial cells cultured with GFAP IR KO astrocytes (Figure 8G).

Normalized glucose uptake in older GFAP-IR KO mice may be related to high peripheral glucose levels found in these mice at young age (Garcia-Caceres *et al.*, 2016). Indeed, young, but not older GFAP-IR KO mice show hyperglycemia (*p<0.05, t-test; Figure 9A). Since high glucose has been hypothesized to alter brain glucose transporters (Leão et al., 2020), we determined whether hyperglycemia, mimicked by culturing astrocytes in 50 mM glucose, modifies expression of GluT1 mRNA and found it increased in control but not in GFAP IR KO astrocytes (***p<0.001, t-test; Figure 9B). Further, brain GluT1 expression in adult, but not young GFAP IR KO or GLAST IR KO mice was within control levels (Suppl Fig 1E). Since high glucose has also been

reported to interfere with the mitogenic activity of astrocytes on endothelial co-cultures (Cohen et al., 2019), we determined HIF1α/VEGF levels in astrocytes grown at different glucose concentrations but did not see any changes (not shown). *(or Suppl Fig 5C including 50 mM glucose),*

IR modulates mitochondrial dynamics in astrocytes.

Since mitochondria modulate angiogenic signaling (Chang et al., 2014; Marcu et al., 2017; Reichard and Asosingh, 2019), and GFAP-IR KO mice show altered mitochondrial function in astrocytes (Garcia-Caceres *et al.*, 2016), we examined whether increased angiogenesis in these mice is related to altered mitochondrial function. We determined levels of reactive oxygen species (ROS) in IR-deficient astrocytes after shIR transfection using H2DCFDA, a ROS sensitive fluorescent dye, and found them increased as compared to control cultures (Figure 9C). Next, we inhibited ROS with N-acetylcysteine (NAC; 10 mM) in shIR-transfected astrocytes (Figure 9C) to determine its role in angiogenic signaling and found normalized HIF-1/VEGF levels (Figure 9D,E). Significantly, treatment of young GFAP IR KO mice with NAC (600 mg/kg, ip) normalized brain blood flow (Figure 9F) and increased brain GSH, an antioxidant defense metabolite significantly decreased in GFAP IR KO mice (**$p<0.01$ and ***$p<0.001$, t-test; Figure 9G).

Increased ROS impairs mitochondrial function (Willems et al., 2015), whereas impaired mitochondria are removed by mitophagy (Twig and Shirihai, 2011). Indeed, shIR-transfected astrocytes showed a decreased mitofussin 2 (Mfn2)/Fis1 ratio, an indicator of increased mitophagy (**$p<0.01$, t-test; Figure 10 A), and increased depolarized mitochondria (**$p<0.01$, t-test; Figure 10B and Suppl Fig 6A), an indicator of the pre-autophagic pool of dysfunctional mitochondria (Elmore et al., 2001) as determined by a fluorescence sensor. ROS also stimulates mitochondria biogenesis (Wenz, 2013), and mitophagy is coupled to this process (Palikaras et al., 2015). Indeed, mitochondrial biogenesis in IR-deficient astrocytes was increased, as determined by increased PGC-1α expression in sh-IR transfected astrocytes (**$p<0.01$, t-test; Figure 10C), or increased Tfam levels -a master regulator of mitochondrial biogenesis (Tiefenbock et al., 2010) in astrocytes obtained from GFAP IR KO mice (**$p<0.01$, t-test; Figure 10D). Since mitochondria-endoplasmic reticulum contacts in reactive astrocytes are involved in vascular remodeling (Gbel et al., 2020), and astrocyte morphology in GFAP IR KO mice resemble reactive astrocytes (Garcia-Caceres *et al.*, 2016), we analyzed mitochondria-associated endoplasmic reticulum membrane (MAM) dynamics since this is the region responsible of the interaction between both organelles. We determined in IR-deficient astrocytes the assembly of the MAM complex formed by the chaperone glucose regulated protein 75 (Grp75) with inositol trisphosphate receptors (IP3R, located in the ER) and voltage dependent anion channel (VDAC, located in the mitochondria). Grp75 tethers IP3R with VDAC and the resulting complex bridges both organelles and is involved in Ca^{++} signaling (Szabadkai et al., 2006). We used PLA to determine the interaction of (Grp75) with IP3R and of Grp75 with VDAC and in this way the degree of contact at the mitochondrial-ER junction (Tubbs and Rieusset, 2016). We found greatly decreased interaction between both pairs of proteins indicating reduced interaction of the two organelles in IR-deficient astrocytes (**$p<0.01$, t-test Figure 10E,F). Collectively, these results indicate that mitochondrial activity is impaired in IR-deficient astrocytes and help explain changes in vasculature.

To determine the impact of altered mitochondrial dynamics in angiogenic signaling/glucose handling by astrocytes lacking IR, mitophagy was inhibited with cyclosporine (5 μM) (Esteban-Martinez et al., 2017), as indicated by a normalized

Mfn2/Fis1 ratio in these cells (Suppl Figure 6B). Cyclosporine normalized HIF-1/VEGF (Suppl Figure 6 C,D) and GluT1 (Suppl Figure 6E) levels in GFAP IR KO astrocytes. Hence, disturbed mitochondrial function in astrocytes with downregulated IR alters markers of angiogenic and glucose metabolism, suggesting that it underlies the observed changes in brain perfusion and glucose uptake.

IR deficient astrocytes show impaired glucose/oxygen sensing

Since mitochondria are involved in O_2 (Hamanaka and Chandel, 2009) and glucose (Stoltzman et al., 2008) sensing, we next examined whether downregulation of IR affects these two mechanisms in astrocytes, as they are also linked to angiogenesis and glucose uptake. We determined in GFAP IR KO astrocytes the levels of TRPA1 channels ((**p<0.01, t-test; Figure 11A) and of NADPH (**p<0.01, t-test; Figure 11B), two O_2 sensors (Takahashi et al., 2011) (Ward, 2008) expressed in astrocytes. We also determined levels of the mitochondrial glucose sensor MondoA/Mlx, a transcription factor in the mitochondrial membrane involved in responses to glucose (Stoltzman *et al.*, 2008), and found it decreased in GFAP IR KO astrocytes (**p<0.01, t-test; Figure 11C). Amelioration of ROS levels with NAC resulted also in normalization of TRPA1, NADPH and MondoA levels (Figure 11A-C). This suggests that excess ROS is involved in decreased levels of O_2 and glucose sensors in IR-defective astrocytes, which probably contributes to altered brain perfusion and glucose uptake.

Functional impact of astrocyte insulin receptor-deficiency

We determined possible impacts on brain function in tamoxifen-regulated GFAP-IR KO mice, as previous observations in mice constitutively lacking astrocyte IR show mood alterations (Cai *et al.*, 2018). Further, uncoupling of blood flow and glucose uptake may affect behavior. We observed modest, gradual changes in mood, with slightly reduced anxiety in young mice that normalized with time (*p<0.05, t-test; Suppl Figure 7A). Other mood traits such as depressive-like behavior also show a time-dependent pattern, with young mice showing normal performance in the tail suspension and forced swim tests, that evolved to significant, moderate lower resilience to both stressful challenges in adult mice (*p<0.05 and **p<0.01, t-test; Suppl Figure 7B, C). GFAP IR KO mice show normal working and spatial memory, as determined in the Y and Barnes mazes, respectively (Suppl Figure 7D,E).

We also determined whether astrocytic IR affects Alzheimer´s pathology, as brain insulin resistance has been proposed to be associated to this condition (Talbot et al., 2012). We crossed GFAP-IR KO mice with APP/PS1 mice, an established model of Alzheimer-like pathology (Citron et al., 1997) and determined plaque load and working memory, two hallmarks of the disease. As shown in Figure 12, compound GFAP-IR KO/APP/PS1 mutants show increased plaque load (*p<0.05, t-test) and greater memory impairment (***p<0.001, t-test) than GFAP IR control/APP/PS1 or APP/PS1 mice.

Discussion

Mice with insulin receptor deficiency in astrocytes have been previously shown to display central and peripheral deficiencies in glucose metabolism and altered behaviors (Cai *et al.*, 2018; Garcia-Caceres *et al.*, 2016). The present observations provide additional evidence that insulin signaling in this type of glial cells is important for brain function. Mice with IR deficiency in astrocytes develop brain insulin resistance, as previous results suggested (Garcia-Caceres *et al.*, 2016), and show uncoupled brain blood flow and glucose uptake. We also observed disturbed mitochondrial function in astrocytes with down-regulated IR signaling, that associates to excess ROS production.

Importantly, mitochondrial dysfunction in IR-deficient astrocytes involved not only previously documented structural and metabolic disturbances (Garcia-Caceres *et al.*, 2016), but also impaired biogenesis, reduced levels of glucose/O_2 sensors and decreased mitochondrial-ER contacts that ultimately affect Ca^{++}signaling. The latter was also observed in POMC neurons of these mice (Garcia-Caceres *et al.*, 2016). When ROS levels or aberrant mitophagy are pharmacologically ameliorated, mitochondrial function is restored, and blood flow is normalized. Our findings provide a molecular framework for the purported relationship between cerebral blood flow and brain metabolism (Koehler *et al.*, 2009), and further substantiate brain blood flow deficits in insulin-resistant states (Rusinek *et al.*, 2015).

The presence of IR in astroglial end-feet, similar to previous observations with the closely related insulin-like growth factor I receptor (Garcia-Segura et al., 1997), provides anatomical support for its actions on the vasculature, as glial end-feet are intricately participating in neuro-vascular coupling (Abbott et al., 2006). Anatomically, large bundles of glial end-feet mitochondria are in close proximity to vessels (Mathiisen *et al.*, 2010), assuring local metabolic support (Agarwal et al., 2017), and, as our results now suggest, angiogenic signals. Previously, we observed changes in mitochondrial morphology and increased autophagic-related organelles in astrocytes lacking IR (Garcia-Caceres *et al.*, 2016). Conceivably, altered angiogenic signaling in GFAP IR KO mice may be the result of altered mitochondrial function, as mitochondria modulate angiogenesis (Chang *et al.*, 2014; Marcu *et al.*, 2017; Reichard and Asosingh, 2019). In agreement with angiogenic actions of astrocyte IR, this receptor in perycites has been reported to control retinal vasculature (Warmke *et al.*, 2021).

An intriguing aspect of our observations is the evolving pattern of glucose/blood flow uncoupling along time that suggests accelerated aging. Uncoupling between brain glucose uptake and perfusion is widely documented in human studies (Abu-Judeh et al., 1998), including healthy old individuals (Fisher et al., 2013). Other instances of uncoupling have been documented under physiological conditions in experimental animals (Devor et al., 2008). However, to our knowledge, glucose uptake is preserved in the face of reduced brain perfusion. Thus, it seems that reduced perfusion can be compensated by increasing glucose uptake, but reduced glucose uptake cannot be compensated by increasing perfusion. A potential explanation of time-dependent changes in this uncoupling is that protracted impairment of central and peripheral glucose handling in GFAP IR KO mice may gradually wear off aberrant angiogenic signaling by astrocytes. Alternatively, sustained mitochondrial injury in the brain of GFAP-IR KO mice due to excess ROS, may eventually result in loss of angiogenic potential. In turn, reduced perfusion in older GFAP IR KO mice is accompanied by slightly increased glucose uptake, a common adaptive mechanism seen in humans. Intriguingly, ApoE4 carriers show a similar age-dependent change in brain perfusion, with higher levels in young adults and lower levels in older individuals (Filippini et al., 2011). Since ApoE4 has been shown to interfere with insulin signaling (Zhao et al., 2017), our results suggest that the underlying mechanism in ApoE4 carriers is impaired IR activity in astrocytes. This possibility will require further study. Conversely, while uncoupling between brain perfusion and glucose metabolism has been reported in prodromal stages in human AD (Leuzy et al., 2018), both processes decay in parallel along progression of the disease (Devous, 2002), making it unlikely that brain insulin resistance in AD patients is the sole responsible of these deficits.

Although circulating insulin plays many important roles in the brain (Fernandez and Torres-Aleman, 2012), the key question of how it reaches its numerous brain targets remains poorly characterized. Early observations documented the presence of insulin in

the cerebrospinal fluid (CSF) and the brain (Margolis and Altszuler, 1967) (Pansky and Hatfield, 1978). Just relatively recently, the origin of brain insulin has been reasonably settled (Gray et al., 2014), including not only a peripheral source, but also low local production (Kuwabara, 2011). Thus, for many years, insulin actions in the brain were assumed to arise exclusively from pancreatic insulin (Schwartz and Porte, 2005) that has to cross the blood-brain-barriers (BBBs) to exert its central actions. Indeed, circulating insulin enters the brain through a saturable transport mechanism (Banks et al., 1997). Whether the insulin receptor in endothelial cells is involved in the process remains controversial, as conflicting results attest (Gray *et al.*, 2017; Konishi et al., 2017; Rhea *et al.*, 2018). However, there are insulin receptors in the cells forming the BBBs; that is, epithelial cells at the choroid plexus (Baskin et al., 1986), brain capillary endothelial cells (Frank et al., 1986) able to transcytose insulin (King and Johnson, 1985), and astrocytes (Baron-Van et al., 1991). Our results suggest that astrocytes act as the gate of entrance of circulating insulin into the brain, as previously hinted (Garcia-Caceres *et al.*, 2016). Once insulin crosses the vessels, it would be taken up by astrocytes that, in turn, will deliver it to neighboring neurons. Thus, circulating insulin reaches its neuronal targets through an astrocyte-neuron pathway. Knowledge of the entire route of entrance of circulating insulin into the brain, including vessel transcytosis, is of great relevance, as in diabetes and in several neurodegenerative diseases brain insulin resistance is a likely pathogenic component. Our results pose astrocytic IRs as important targets for future studies in the search of novel therapeutic options for brain insulin resistance.

Indeed, GFAP IR KO develop brain insulin resistance, as attested by blunted brain IR activation, reduced capture of circulating insulin, and loss of astrocyte responses to systemic insulin. In turn, depression has long been associated to insulin resistance (Moulton et al., 2015; Rasgon and Kenna, 2005; Watson et al., 2018). As previously reported in a Cre/Lox model of constitutive IR deletion in astrocytes (Cai *et al.*, 2018), we found that GFAP IR KO mice show a depressive phenotype. However, in our tamoxifen-regulated IR ablation model, where IR activity was deleted in adulthood, mood dysregulation appears at later age. While in the constitutive model, mood dysregulation was linked to dopaminergic function and could be corrected by central administration of ATP analogs (Cai *et al.*, 2018), the possible contribution of blood flow/glucose uptake uncoupling to development of mood disturbances should be explored in future studies. Since hyper-perfusion is no longer present at the time that mice start developing depressive-like behavior, we speculate that hyper-perfusion refrains development of depression. Indeed, at young age, GFAP IR KO mice display lower levels of anxiety, which could deter development of depressive-like behavior.

This study contains several limitations. For instance, both the PET and SPECT radiotracers used in this study are redox sensitive (Maulucci et al., 2016a), which could interfere with the interpretation of changes in glucose uptake and blood flow, respectively. However, increased oxidative stress is associated with increased PET and decreased SPECT signal, respectively (Maulucci *et al.*, 2016a), making it unlikely that the observed decreased PET and increased SPECT signatures observed are related to increased ROS production by IR-deficient astrocytes. Finally, changes in SPECT and PET signatures correlated with angiogenic markers and GluT1 levels, respectively, providing additional support to the validity of the measurements.

In summary, brain insulin resistance associates to increased ROS production, mitochondrial disturbances and interferes with functional hyperemia, resembling changes seen during brain aging. These results adds to the multitasking role of astrocytic IR, including regulation of peripheral glucose metabolism (Friesen et al.,

2016), gliotransmission, dopaminergic activity, mood homeostasis (Cai *et al.*, 2018), and control of gonadal function (Manaserh et al., 2019). Boosting IR function in astrocytes may be of therapeutic value in neurodegenerative diseases with altered tissue perfusion and hypo-metabolism.

Materials and Methods

Animals: Wild type 6 months-old male mice (C57BL6/J) were used in EM experiments. Mice with insulin receptors ablated in GFAP (GFAP IR KO mice) or GLAST astrocytes (GLAST-IR KO mice) under regulation of tamoxifen were generated as described in detail before (Garcia-Caceres *et al.*, 2016), by crossing hGFAP-CreER^{T2} or GLAST-CreER^{T2} on a C57 BL/6J background (FM Vaccarino, Yale Univ) with IR$^{f/f}$ mice having the IR gene flanked by loxP sites (R Kahn, Joslin Diabetes Center). Mice with IGF-I receptors ablated in GFAP astrocytes under the regulation of tamoxifen were obtained by crossing IGF-IR$^{f/f}$ mice (B6, 129 background; Jackson Labs; stock number: 012251) with CreERT2.GFAP mice (C57B&/6xSJL/J mix background; Jackson Labs, stock number: 012849, see (Ganat et al., 2006) for further details). Intraperitoneal injection of tamoxifen for 5 consecutive days (75 mg/kg) to adult mice (4-5 weeks old) eliminated IR or IGF-IR specifically in astrocytes, as reported (Garcia-Caceres *et al.*, 2016). Controls received vehicle injections (corn oil). GFAP IR KO mice showed significantly decreased levels of IR in brain, as compared to controls injected with the vehicle (Suppl Figure 3A). GFAP/GLAST IR KO mice were genotyped using PCR protocols already detailed (Garcia-Caceres *et al.*, 2016). Multiplex PCR for GFAP IGF-IR KO genotyping included a common forward primer (P3, 5'−CTG TTT ACC ATG GCT GAG ATC TC−3') and two reverse primers specific for the wild-type (P4, 5'−CCA AGG ATA TAA CAG ACA CCA TT−3') and mutant (P2, 5'-CGC CTC CCC TAC CCG GTA GAA TTC-3') alleles. Mice had access to food and water *ad libitum* and were kept under light/dark conditions. Animal procedures followed European (86/609/EEC & 2003/65/EC, European Council Directives) guidelines and studies were approved by the respective local Bioethics Committees.

Reagents: The following reagents were used: tamoxifen (Sigma, Darmstadt, Germany), Insulin (Sigma), IGF-1 (PreproTech, Rocky Hill, NJ, USA), and tomato lectin-FITC (Sigma). Antibodies used were: Phosphotyrosine (clone PY20, BD Transduction laboratories, San Jose, CA, USA), GFAP (Dako, Glostrup, DK), NeuN (Millipore, Darmstad, Germany), Digoxigenin (Roche Diagnostics, Mannheim, Germany), Insulin receptor ß (Santa Cruz Biotechnology, Dallas, TX, USA), IGF-1 receptor ß (Cell Signaling Technology, Danvers, MA, USA) and ß-actin (Sigma). Antibody to phospho-AKT (Ser^{473}) was from Cell Signalling. AKT1/2 (H-136), was obtained from Santa Cruz Biotechnology. Antibody to Cre-recombinase was from Millipore. Hoechst 33342 was purchased from Invitrogen (Waltham, MA, USA).

Cranial window surgery for *in vivo* imaging: Chronic glass-covered cranial windows were implanted at least 2 weeks before the beginning of the in vivo calcium imaging of astrocytes (Figure 3A). Briefly, mice were anesthetized (isoflurane, 5% for induction, 1.5% for maintenance via nose cone) and placed on a stereotaxic frame. Dexamethasone (0.2 mg/kg) and carprofen (5 mg/kg) were administered. A 4 mm-diameter craniotomy was performed with a pneumatic dental drill over the somatosensory cortex. A stereotaxic microinjection (400 nl; 30 nl/min) of AAV2/5-P$_{GFAP}$-Lck-GCaMP6f (PENN Vector Core; viral titer 6.13 x 10^{13}) was made. A round glass coverslip (5 mm) was laid over the dura mater, covering the exposed brain and part of the skull and glued to the latter with cyanoacrylate-based glue. A layer of dental acrylic was then applied throughout the skull surface and up to the edges of the coverslip. A titanium bar (9.5 ×

3.2 × 1.1 mm) was embedded in the dental acrylic to secure the mouse onto the stage of the microscope for imaging.

Ca^{2+} imaging: Imaging of GCaMP6f-expressing astrocytes was performed with a two-photon laser scanning microscope, custom-modified with a femtosecond laser (Chameleon Ultra II, Coherent Inc) and ScanImage 3.8 software written in MATLAB (MathWorks; RRID:SCR_001622), under isoflurane anesthesia (1%–1.5%). Mice were secured to the microscope using the titanium head bar. A 10X immersion objective (numerical aperture, NA, of 0.45, Nikon) was used to create a map of the area of interest and a 40X water-immersion objective (NA=1.1) was used for visualization of individual areas. Excitation of GFP was achieved by tuning the laser at 780 nm with a power at the sample of < 20mW. After two weeks of surgery and viral injection, specific expression of constructs in the astrocytes was confirmed by immunostaining. Images were acquired every 1.4-1.7 seconds and ROIs were designed with ImageJ in a semi-automated manner using the GECIquant program. Ca^{2+} variations were estimated as changes of the fluorescence signal over baseline ($\Delta F/F_0$), and regions of interest were considered to respond to the stimulation when $\Delta F/F_0$ increased three times the standard deviation of the baseline. The astrocyte Ca^{2+} signal was quantified from the Ca^{2+} oscillation frequency. The time of occurrence was considered at the onset of the Ca^{2+} spike. Custom-written software in MATLAB (MATLAB R2016; Mathworks, Natick, MA) was used for computation of fluorescence of each ROI.

Cell cultures and transfections: Cultures were done as previously described in detail (Fernandez *et al.*, 2017). For astroglial cultures, postnatal (day 3–4) brains from control and GFAP IR KO mice were dissected, cortex and hippocampus removed, and mechanically dissociated. The resulting cell suspension was centrifuged and plated in DMEM/F-12 (Life Technologies) with 10% fetal bovine serum (Life Technologies) and 100 mg/ml of antibiotic-antimycotic solution (Sigma-Aldrich, Spain). After 15–20 days, astrocytes were re-plated at 1.2×10^5 cells/well. To downregulate IR expression in astrocytes obtained from GFAP IR KO mice, OH-tamoxifen (1µM) or the vehicle were added and cultures were used after 48 h, when IR levels were reduced. Endothelial cell cultures were performed as described (Perriere et al., 2005) with modifications (Munive et al., 2019). Briefly, dissection was performed on ice and cortices were cut, and digested in a mixture of collagenase/dispase (270 U collagenase/ml, 0.1% dispase) and DNAse (10 U/ml) in DMEM (Life Technologies) for 1.5 h at 37°C. The cell pellet was separated by centrifugation in 20% bovine serum albumin/DMEM (1000g, 15 min) and incubated in a collagenase/dispase mixture for 1 h at 37°C. Capillary fragments were retained on a 10µm nylon filter, removed from the filter with endothelial cell basal medium (Life Technologies), supplemented with 20% bovine plasma-derived serum and antibiotics (penicillin, 100 U/ml; streptomycin, 100 µg/ml), and seeded on dishes coated with collagen type IV (5 µg/cm^2). 3µg/mL puromycin was added for 3 days. Puromycin was then removed from the culture medium and replaced by fibroblast growth factor (2 ng/ml) and hydrocortisone (500 ng/ml).

For transfection, astrocytes were electroporated (2×10^6 astrocytes with 2 µg of plasmid DNA) before seeding using an astrocyte Nucleofector Kit (Amaxa, Lonza, Switzerland). After electroporation, cells were plated to obtain a final cell density on the day of the experiment similar to that obtained with the transfection method. The transfection efficiency was 60–80%, as assessed with a GFP vector expression.

Insulin administration: Mice were anesthetized with isofluorane with oxygen flux at 0.8–1 l/min. The common carotid artery was exposed, and the external carotid ligated. A guide cannula was inserted in the common carotid artery and 100µl Dig-insulin was injected using a Hamilton syringe coupled to a nanoinjector. After 1 hour, mice were

perfused with saline and 4% paraformaldehyde. Brains were removed and processed for immunohistochemistry. For IR phosphorylation experiments, mice were injected with 5 IU insulin intraperitoneally (100 µl, 1 hour) or intra-parenchyma (2 µl, 15 min). For the latter, a Hamilton micro-syringe was inserted in the left lateral somatosensorial cortex with the following coordinates: 1.7 mm posterior and 1 mm lateral relative to bregma (left hemisphere), and 0.8 mm down the skull surface. Mice were then perfused with saline and brain and skeletal muscle isolated, frozen until assayed by IR immunoprecipitation and Western blotted with anti-pTyr.

Digoxigenin-labeled insulin: 100 µl of 1 mg/ml recombinant human insulin (Sigma) was mixed with 1 ml of PBS pH 8.5. Digoxigenin-3-O-methylcarbonyl-ε-aminocaproic acid-N-hydroxysuccinimide ester (NHS-Dig; Roche Diagnostics) dissolved in dimethyl sulfoxide (DMSO) was added to the insulin solution at a molar ratio of 1:5. After incubation at room temperature for 2 h, non-reacted NHS-Dig was removed by a Sephadex G-25 column (GE Healthcare, Chicago, IL, USA). Digoxigenin-labeled insulin (Dig-insulin) was stored at -20°C until use.

Immunofluorescence: Immunolabeling was performed as described (Fernandez et al., 2012). Mice were deeply anesthetized with pentobarbital (50 mg/kg), and perfused transcardially with saline followed by 4% paraformaldehyde in 0.1 M phosphate buffer, pH 7.4 (PB). Saline perfusion was intended to eliminate insulin binding to brain vessels. Brains were then dissected, and coronal 50-µm-thick brain sections were cut in a vibratome and collected in PB. Sections were incubated to block non-specific antibody binding, followed by incubation overnight at 4°C with the primary antibodies in PB - 1% bovine serum albumin - 1% Triton X-100 (PBT). After several washes in PBT, sections were incubated with the corresponding Alexa-coupled secondary antibody (1:1000, Molecular Probes, ThermoFisher Scientific) diluted in PBT. Again, three 5-minute washes in PBT were required. Slices were rinsed several times in PB, mounted with gerbatol mounting medium, and allowed to dry. For endothelial cell staining, sections were incubated with Tomato lectin-FITC overnight at 4ºC followed by several washes in PBT. Omission of primary antibodies was used as control. Confocal analysis was performed in a Leica microscope (Wetzlar, Germany).

Proximity ligation assays (PLA): Assays were run using the Duolink® In Situ Detection Reagents Red Kit (DUO92008, Merck) as described before (Martinez-Rachadell et al., 2019). Brain slices were incubated with 1% Triton X-100 phosphate-buffered saline (PBS-T) filtered solution during 5 minutes. To remove Triton X-100, slices were washed 3 times in PBS (5 min each wash) and incubated with filtered glycine 20mM/PBS 0.1M for 10 minutes at room temperature (RT). hereafter, the solution was removed and the slices were placed over gelatin-coated microscope slides and 30 µl of Duolink blocking solution (1X) were added per section and incubated 1 hour at 37ºC inside a pre-heated humidity chamber. Slices were then incubated overnight at 4ºC with primary antibodies diluted in Duolink blocking solution (1x). Negative controls were only treated with G5 primary antibody. The next day, slices were washed twice (5min each) with buffer A and then incubated for 1 hour at 37ºC with Duolink secondary antibodies (PLA probes). Slices were again washed with buffer A solution 3 times at room temperature (5min each) and incubated with a mixture of ligation buffer (1:5) and ligase (1:40) both diluted in DNAse-free water. The ligation reaction was left 30 minutes at 37ºC, and slices were then washed twice with buffer A, and the amplification reaction was performed. Then, sections were incubated for 100 minutes at 37ºC with a mixture of Duolink amplification buffer (1:5) and polymerase (1:80) both diluted in DNAse-free water. Two 10-minute washes with Buffer B were performed. Sections were fixed for 10 min at room temperature with 4%

paraformaldehyde solution and washed 3 times in PBS (5 min each). Thereafter, GFAP immunocytochemistry was performed. PLA puncta were scored using the Imaris software with images taken at 63X objective in a confocal microscope. For counting, a surface was created in the green channel to select all $GFAP^+$ cells. Next, 10µm diameter spots were created in the blue channel to select the nuclei on that surface, obtaining the total number of $GFAP^+$ cells. Finally, a second spot was created in the red channel (1µm diameter) to select all the PLA points present on the previously created surface. The ratio of PLA points/$GFAP^+$ cell was then calculated.

Vessel density: Images were taken at 40X on a Leica confocal microscope from coronal sections (50µm) of mouse brain cortex. Using IMARIS 9.6.0 software, a 3D surface was created in the green channel thus selecting all vessels. The surface covers the entire thickness of the section. We selected "average values" in the control panel to obtain the data for the volume of the vessels (µm3). This volume corresponds to the 3D surface created and is directly proportional to the volume of vessels. Images were scored blinded.

Quantitative PCR: Total RNA isolation from brain tissue was carried out with Trizol. One mg of RNA was reverse transcribed using High Capacity cDNA Reverse Transcription Kit (ThermoFisher Scientific, Waltham, MA, USA) according to the Manufacturer's instructions. For quantification of specific genes, total RNA was isolated and transcribed as above and 62.5 ng of cDNA was amplified using TaqMan probes for mouse IGF-1receptor (IGF-1R) and Insulin receptor (InsR), and rRNA 18S as endogenous control (ThermoFisher Scientific). Each sample was run in triplicate in 20 µL of reaction volume using TaqMan Universal PCR Master Mix according to the manufacturer's instructions (ThermoFisher Scientific). All reactions were performed in a 7500 Real Time PCR system (ThermoFisher Scientific). Quantitative real time PCR analysis was carried out as described (Pfaffl, 2001). Results were expressed as relative expression ratios on the basis of group means for target transcripts versus reference 18S transcript. At least five independent experiments were done.

Immunoprecipitation and Western blotting: Assays were performed as described (Fernandez et al., 2007). Brain tissue was homogenized in ice-cold buffer with 10mM Tris HCl pH 7.5, 150mM NaCl, 1mM EDTA, 1mM EGTA, 1% Triton X-100, 0.5% NP40, 1mM sodium orthovanadate, and a protease inhibitor cocktail (Sigma) plus 2mM PMSF, using 1 ml of buffer per mg of tissue. Insoluble material was removed by centrifugation, and supernatants were incubated overnight at 4 ºC with the antibodies. Immunocomplexes were collected with Protein A/G agarose (Santa Cruz Biotechnology) for 1 h at 4 °C and washed 3X in homogenization buffer before separation by SDS-polyacrylamide gel electrophoresis and transferred to nitrocellulose membranes. After blocking for 1 h with 5% BSA in TTBS (20 mM Tris-HCl, pH 7.4, 150 M NaCl, 0.1% Tween 20), membranes were incubated overnight at 4 ºC with the different antibodies in TTBS, washed, incubated with secondary antibodies and develop using the Odissey procedure (Li-Cor Biosciences, Lincoln, NE, USA).

Immunoelectron microscopy: Immunogold procedure was performed as previously described (Gomez-Arboledas et al., 2018)**.** After deep anesthesia with sodium pentobarbital (60 mg/kg), 6 month-old male mice (C57BL6/J) were perfused transcardially with 0.1 M phosphate-buffered saline (PBS), pH 7.4 followed by fixative solution containing 4% paraformaldehyde, 75 mM lysine and10 mM sodium metaperiodate in 0.1 M PB, pH 7.4. Brains were removed, post-fixed overnight in the same fixative solution at 4°C, coronally sectioned at 50 µm thicknesses on a vibratome (Leica VT1000S), and serially collected in wells containing cold PB and 0.02% sodium azide. For IGF-1R or IR immunogold labelling, sections containing the somatosensory

cortex were used. Sections were first washed with PBS and incubated in a 50 mM glycine solution 5 minutes to increase antibody binding efficiency. Following a standard immunohistochemical protocol, tissue was first free-floating incubated in a rabbit polyclonal anti-IGF-IRα antibody or a anti-IR antibody in a PBS 0.1M/1% BSA solution for 48 hours at 22ºC. Then, sections were washed in PBS, and incubated with 1.4 nm gold-conjugated goat anti-rabbit IgG (1:100; Nanoprobes) overnight at 22ºC. After post-fixing with 2% glutaraldehyde and washing with 50 mM sodium citrate, labelling was enhanced with the HQ Silver^{TM} Kit (Nanoprobes), and gold toned. Finally, immunogold labelled sections were fixed in 1% osmium tetroxide, block stained with uranyl acetate, dehydrated in acetone, and flat embedded in Araldite 502 (EMS, USA). Selected areas were cut in ultrathin sections (70-80 nm) and examined and photographed with a JEOL JEM1400 electron microscope. As a control for the immunogold technique, sections were processed as above but omitting the primary antibody. No specific labelling was observed in these control sections.

SPECT/CT Imaging: Wild type (wt) and APP/PS1 transgenic mice were imaged by SPECT/CT at the Brain Imaging Unit of the Cajal Institute (CSIC). Awake mice were iv injected with ^{99m}Tc-HMPAO (exametazine, Iba Molelular, Madrid, Spain) via a catheter inserted in the tail vein, in a volume of 0.2 ml. An ISOMED 2010 dose calibrator (activity interval 1 μCi-1350 mCi, in the case of ^{99m}Tc) was used to calibrate radiotracer doses. Thirty minutes after the injection of the radiotracer (32-42 MBq), to allow its biodistribution, mice were anesthetized with isoflurane (4% induction, 2% maintenance) in O_2 (0.7 l/min). SPECT and CT images were acquired with a bimodal Albira SPCT/CTpreclinical imaging system (Bruker). All SPECT acquisitions were made with FOV of 40 mm, comprising the head, for 30 min, with a single-pinhole collimator, and 60 projections of 60 sec each. This was followed by a 10 min CT scan (quality Best, capture mode step & shoot, 600 projections, voltage 45 kV and intensity 400 μA). The SPECT/CT scans were reconstructed with OSEM algorithm (5 subsets, 2 iteractions) and FBO, respectively, with the Albira suite Reconstructor software (Carestream Molecular Imaging). SPECT and CT images were fused and analyzed using PMOD software (Biomedical Imagen Quantification, Basel, Switzerland). Activity was quantified by matching the CT image of the skull of each animal to a common magnetic resonance (MR) mouse brain template, in which regions of interest (ROI) were previously delineated, according to Ma et al. (Polavarapu et al., 2005). After saving the spatial transformation, it was applied to the corresponding fused SPECT image, to allow the correct co-registration to the MR brain template. Results were normalized to the actual radioactivity dose injected and the body weight of each animal (Kuntner et al., 2009). All these processes were carried out with PMOD software version 3.0 (PMOD Technologies, Switzerland). Alternatively, ROI activity uptake was expressed as the percentage injected activity (%ID). Results are mean ± SEM.

^{18}F-FDG PET imaging: ^{18}F-FDG PET was used to measure brain glucose handling as described in detail before (Hernandez-Garzon *et al.*, 2016). ^{18}F-FDG uptake in the different brain regions was calculated in kBq/cc units.

ROS imaging: Brain ROS levels were visualized following previously published procedures with some modifications (Behrens et al., 2007). Briefly, DHE (Dihydroethidium, D11347, Invitrogen) solution (1.25 mg/mL) was freshly prepared in anhydrous DMSO under low-flow nitrogen gas in the dark. Just before injection, DHE solution was mixed with an equal volume of sterile saline, and injected intraperitoneally in two doses of 20 mg/Kg separated by 30 min. After 18 h, mice were intracardially perfused with 4% PFA. The brains were removed and postfixed in 4% PFA. Following 24 h, images were acquired *ex vivo* with an IVIS Spectrum instrument (Xenogen)

(excitation filter, 518 nm; emission filter, 605 nm; exposure time, 1 s; bin, 8; f/stop, 2). Image analysis was performed by drawing a ROI around the whole brain and recording the mean pixel intensity using IVIS Lumina software. Results were plotted as mean pixel intensities using Graphpad Prism 4.

Biochemical assays The NAPDH/NAPD ratio in astrocytes obtained from GFAP IR KO mice was calculated…….. ROS levels in sh-RNA transfected astrocytes was determined……GSH levels in GFAP IR KO astrocytes were assessed using…..

JC-1 flow cytometry: Astrocytes were nucleofected with IR siRNA or a siRNA with a random sequence (siRNA scramble) as control and were grown in normal conditions for 3-4 days and then incubated for 5 minutes in the presence of JC1. Cells were washed and harvested with trypsin. JC1 staining was assayed by flow cytometry. Side scatter analysis and Propidium Iodide was used to discard death cells and gate selection.

Statistics: Statistical analysis was performed using GraphPad Prism 5.0 (La Jolla, CA, USA). To compare differences between two groups, Student's t-test (Gaussian distribution of data) or Mann–Whitney or Wilcoxon tests (non-Gaussian distribution of data) were used. To compare multiple variables, two-way ANOVA was used, followed by a Bonferroni post hoc test to compare replicate means or Kruskal–Wallis test when the data did not follow a normal distribution. Statistical differences were considered when $p < 0.05$. Results are presented as mean ± SEM.

Acknowledgements

We are thankful to M. Garcia and R. Cañadas for technical support. This work was funded by a grant from Ciberned, an Inter-CIBER project (PIE14/00061), forms part of the project PID2019-104376RB-I00 (ITA) funded by MCIN/AEI/10.13039/ 501100011033, and grant PI18/01557 (to AG) from Instituto de Salud Carlos III (ISCiii) of Spain (co-financed by FEDER funds from European Union).
. JAZ-V acknowledges the financial support of the National Council of Science, Technology and Technological Innovation (CONCYTEC, Perú) through the National Fund for Scientific and Technological Development (FONDECYT, Perú).

Author´s contributions

MEFdS performed and designed experiments, analyzed results, participated in discussion of results, and wrote parts of the manuscript. JP performed and designed experiments, analyzed results, participated in discussion of results, and wrote parts of the manuscript. JAZV performed experiments, analyzed results, and wrote parts of the manuscript. PM designed and conducted experiments, interpreted results, participated in discussion of results, and wrote part of the manuscript. AN designed and performed experiments, analyzed results, and wrote parts of the manuscript. ITA designed the study, analyzed and interpreted results, and wrote the manuscript.

Competing interest

No competing interests to declare

LEGENDS TO FIGURES

Figure 1: IR is expressed by astrocyte end-feet. A, Electron microscopy photograph using immuno-gold labeling for IR illustrating the presence of immunoeractive IR deposits in astroglial end-feet surrounding brain capillaries and in endothelial cells. **B,** A1 and A2 squares from A, are shown at greater magnification. Note the presence of IR gold particles in endothelial cells (red arrows) and astrocytic end-feet (black arrows). Bar in A is 2 µm, and in B, 0.5 µm.

Figure 2: Systemic injection of insulin stimulates IR phosphorylation in cortex. A, Intraperitoneal injection of insulin (5 U/ml) results in stimulation of IR in the mouse somatosensory cortex as compared to control mice (injected with the same amount of saline; t-test, t= , $p<0.05$). **B,** Ablation of IR in GFAP IR KO astrocytes after tamoxifen administration results in markedly reduced activation of cortical IR after systemic insulin in comparison to vehicle (corn oil) injected mice (t-test, t= , $p<0.05$). **C,** In these animals, activation of muscle IR was intact, as compared to oil-injected GFAP IR KO mice. Activation of IR is shown as amount of Tyrosine phosphorylated receptor (pTyr) normalized by total levels of immunoprecipitated IR. Representative blots are shown. Quantification of changes is shown in histograms (n=8 for each group). *$p<0.05$, **$p<0.01$ and ***$p<0.001$ in this and following figures.

Figure 3: *In vivo* two-photon imaging of activity of GCaMP6-labeled astrocytes. A, Mouse bearing a cranial window (left), and a macroscopic image of the mouse cranial window (right). **B,** Representative two-photon fluorescence intensities for viral transfection of AAV5-P_{GFAP}-Lck- GCaMP6f in somatosensory cortex imaging *in vivo*. Note astrocytic endfeet enwrapping blood vessels. Scale bar, 35 µm. **C,** Left, Representative experiments showing the amplitude of calcium events versus time 5 min before (basal) and 15 min after ip injection of insulin (3 IU/kg body weight) in Control littermates (top), and GFAP IR KO (bottom) mice. Right, Representative raster plot of ROIs activity versus time showing the frequency of calcium events 5 min before (basal) and 15 min after injection of insulin in Control (top) and GFAP IR KO (bottom) mice. **D,** Changes of spike frequency of Ca^{2+} signals per area 5 min before (basal) and 15 min after i.p. injection of insulin in Control (n = 12 from n = 4 mice, $p<0.01$ Wilcoxon test) and GFAP IR KO (n = 19 from n = 4 mice, $p= 0.163$ Wilcoxon test) mice. Differences between groups were determined by Kruskal–Wallis test (**$p<0.01$).

Figure 4: Insulin receptors in astrocytes are required for neurons to capture circulating insulin. A, Intra-carotid injection of digoxigenin-labeled insulin (Dig-insulin) results in its neuronal accumulation only when astrocytes express IR (no tamoxifen). Panel a shows astrocyte end-feet ($GFAP^+$ in green) ensheathing brain capillaries in control (-tamoxifen) mice receiving Dig-insulin injections. No Dig staining is seen. In contrast, Dig staining is seen in cell of panel b (white dotted square) with neuronal morphology (red), that are magnified in panel c (white asterisks). **B**, Accumulation of labeled insulin is readily seen in hippocampal neurons ($NeuN^+$ cells) of control mice (no tamoxifen). **C,** GFAP IR KO mice (treated with tamoxifen) do not show Dig staining in neurons after intracarotid injection of Dig-insulin. In panel a, vessels surrounded by $GFAP^+$ astroglial end-feet show abundant digoxigenin staining, suggesting lower transfer of Dig-insulin into the brain. In panels b and c (higher magnification of dotted white square in b) neuronal-like shapes with Dig staining are absent. Note the pronounced GFAP reactivity of astrocytes as compared to panel c in

A. **D,** GFAP IR KO (+ tamoxifen) do not show $NeuN^+$ (green) cells co-labelled with Dig in the hippocampal granular cell layer. Green: $GFAP^+$ or $NeuN^+$ cells; Red: $Digoxigenin^+$ cells.

Figure 5: Brain perfusion and glucose uptake in GFAP IR KO. A, Brain perfusion, as determined by brain ^{99m}Tc-HMPAO accumulation, is significantly increased in young (3 months-old, upper histograms) GFAP-IR KO mice (receiving tamoxifen) as compared to controls (vehicle), while in adult mice (>1 year-old, lower histograms), brain perfusion becomes significantly decreased (n=9-10 per group; t-test, t= ; **p<0.01). A representative SPECT image taken from young mice is shown. **B,** Brain glucose uptake, as determined by ^{18}F-FDG, was significantly decreased in young GFAP-IR KO mice, while in older GFAP-IR KO mice, brain uptake was slightly increased over controls (n= 5-9 per group; t-test, t= ; ***p<0.001). A representative PET image taken from young mice is shown.

Figure 6: Brain vasculature in GFAP IR KO mice. A, Brain levels of von Willebrandt factor (vWF), a marker of vascularity (Thomas *et al.*, 2015), are increased in young GFAP IR KO mice, while in older mice remain at control levels (n= 10; t-test, t= , *p<0.05). **B,** Vessel volume in brain of young, but not adult GFAP IR KO is increased (n= ; t-test, t= , **p<0.01). Vessels were identified with FITC-labelled tomato lectin and quantified (right histograms). Note greater vascularity in adult controls than in young ones, in agreement with increased perfusion seen by SPECT imaging in Figure 5. **C,** Sirt-1 mRNA levels are significantly increased in the brain of GFAP IR KO mice (n= ; t-test, t= , **p<0.01).

Figure 7: Angiogenic markers change along time in the brain of GFAP IR KO mice. A-B, Protein levels of HIF-1a and VEGFa were increased in young (A) but not in adult GFAP IR KO mice (B) (n= ; t-test, t= , *p<0.05 and ***p<0.001). **C,** Expression of TGFβ3, Errb2, VEGFa and VEGFc was increased in young GFAP IR KO mice (n= ; t-test, t= , **p<0.01). **D,** In older GFAP IR KO mice (>12 months), expression levels of TGFβ3, Errb2, and VEGFc were normal whereas VEGFa was significantly decreased (n=10; t-test, t= , *p< 0.05).

Figure 8: Angiogenic signaling is increased in astrocytes with reduced IR. A, Levels of VEGFa are reduced in astrocytes with low IR levels. Representative blot and quantitation histogram. Actin is used to normalize protein load (n= ; t-test, t= , **p<0.01). **B,** Similarly, HIF1α levels are increased in IR-deficient astrocytes (n= ; t-test, t= , **p<0.01). **C,** Expression of VEGFa and TGFβ3 is inreased in IR-deficient astrocytes (n= ; t-test, t= , *p<0.05 and **p<0.01). **D,** HIF1α levels are increased in in GFAP IR KO astrocytes- control endothelia co-cultures (n= ; t-test, t= , **p<0.01). **E,** VEGFa levels are increased in GFAP IR KO astrocytes- control endothelia co-cultures (n= ; t-test, t= , **p<0.01). **F,** CD31levels in GFAP IR KO astrocytes- control endothelia co-cultures were significantly increased compared to control astrocytes (n= ; t-test, t= , ***p<0.001). **F,** CD31 staining of endothelial cells from GFAP IR KO mice is more pronounced as compared to endothelia from control littermates.

Figure 9: Glucose and ROS in astrocyte IR deficiency. A, Blood glucose levels are elevated in young (left), but not adult (right) GFAP IR KO mice as compared to littermates (n=5-6 per group; t-test, t= , *p<0.05). **B,** High glucose elevates expression of GluT1 in wild type astrocytes, but not in astrocytes from GFAP IR KO mice (n= ; 2-

way ANOVA, F= ; p<0.001). **C,** ROS levels are increased in astrocytes with knock down IR after transfection with shRNA (see suppl Fig 4B). ROS was detected with the fluorescent marker DHFDA. Representative photomicrographs and quantitation histograms (n= ; t-test, t= ; **p<0.01). Treatment of shIR astrocytes with n-acetylcysteine (NAC) resulted in normalization of ROS, as compared to scramble-treated astrocytes (n=). **D, E,** NAC also normalized HIF1α (D) and VEGF € levels in shIR astrocytes. **F,** In vivo treatment with NAC normalizes blood flow in GFAP IR KO mice (n= ; **p<0.01). **G,** GSH levels in the brain of GFAP IR KO mice were elevated and normalized by NAC treatment (n= ; 2-way ANOVA, F= ; **p<0.01 and ***p<0.001). Note increased GSH after NAC in control brains.

Figure 10: Anti-oxidant treatment normalizes altered mitochondrial dynamics in IR-deficient astrocytes. A, The ratio of mitofusin 2 (Mfn2, a marker of mitochondrial fusion) and fissin1 (Fis1, a marker of mitochondrial fission) is decreased in IR-deficient astrocytes (n= ; t-test, t= ; **p<0.01). **B,** Relative quantification of mitochondrial depolarization determined as red JC1/Green JC1 ratio in siRNA scramble (n=3) and siRNA IR (n=8) cultures (normalized to control conditions) show higher mitochondria depolarization in the latter. (Two-tail t-test, t= ; **p<0.01). **C,** The mitochondrial biogenesis marker PGC-1α is increased in IR-deficient astrocytes (n= ; t-test, t= ; **p<0.01). **D,** IR-deficient astrocytes derived from GFAP IR KO mice show decreased levels of TFAM (n= ; t-test, t= ; **p<0.01). **E-F,** PLA reveals decreased interactions of GFP75 with IP3R (E) (n= ; t-test, t= ; **p<0.01) and VDAC (F) (n= ; t-test, t= ; **p<0.01). Representative images are shown from control (scramble) and IR-deficient (sh-RNA IR) astrocytes ($GFAP^+$ cells, green). Histograms show the ratio of PLA puncta per $GFAP^+$ cell. Nuclei staining with DAPI. Bar is 40 µm.

Figure 11: Glucose and oxygen sensing in IR-deficient astrocytes. A, TRPA1 levels are reduced in IR deficient astrocytes, and are normalized by treatment with NAC (n= ; t-test, t= ; **p<0.01). **B,** NAPDH levels are reduced in IR-deficient astrocytes and normalized after NAC treatment (n= ; t-test, t= ; **p<0.01). **C,** Levels of MondoA are reduced in IR-deficient astrocytes and normalized by NAC (n= ; t-test, t= ; **p<0.01). Representative blots and quantitation histograms shown.

Figure 12: Alzheimer´s-like pathology is exacerbated in GFAP IR KO mice. A, Amyloid plaques were slightly but significantly increased in GFAP IR KO/APP/PS1 mice as compared to controls. Representative photomicrographs showing amyloid plaques (red). Histograms show number of plaques/μm^2? (n= ; 2-way ANOVA, F= ; *p<0.05). **B,** Performance in the Y maze, a measure of working memory was significantly deteriorated in GFAP IR KO APP/PS1 mice as compared to control groups (n= ; 2-way ANOVA, F= ; ***p<0.001 and ***p<0.001***p<0.001).

Supplementary Figure 1: **A,** Brain IR levels are reduced in GFAP IR KO mice as compared to controls (oil-injected). Representative WB is shown (n= ; t-test, t= ; p<0.01). **B,** Intra-parenchymal injection of insulin (U/) to GFAP IR KO mice stimulates Tyrosine phosphorylation of IR (pTyr) to the same degree than vehicle-injected littermates. Representative blot and quantitation histogram. **C,** Systemic injection of IGF-I (1 ug/g) elicits Tyr phosphorylation of the IGF-I receptor in the brain of GFAP IR KO mice similar to vehicle-injected controls. Representative blot is shown. **D,** Brain vessels ensheathed with astrocytic end-feet (GFAP staining in green) do not show accumulation of Dig-ins (DIG, in red) after intracarotid injection in control GFAP-IR KO mice (oil injected, upper picture), while in mice lacking astrocytic IR after administration of tamoxifen (lower picture), DIG label is patent. **E,** mRNA levels of GluT-1 in brain of young GFAP IR KO (left histograms) or GLAST IR KO (lower histograms) mice is significantly decreased, whereas in adult GFAP IR KO mice GluT-1 mRNA levels are normalized (n= ; t-test, t= ; ***p<0.001).

Supplementary Figure 2: **A**, Brain perfusion determined by brain ^{99m}Tc-HMPAO uptake did not change in control littermates along age. **B**, Brain perfusion was decreased in adult GFAP IR KO mice as compared to young ones (n= ; t-test, t= ; **p<0.01). **C,** Brain perfusion remains normal in GFAP IR KO mice given tamoxifen at 1 year of age**. D-E**, Brain glucose uptake determined by ^{18}F-FDG did not change along age in control littermates (D) whereas in GFAP IR KO mice showed a significant increase (E) (n= t-test, t= **p<0.01 vs respective control group).

Supplementary Figure 3: **A,** Brain perfusion in GFAP IGF-IR KO mice is not altered as compared to vehicle-injected controls (n=5-6 per group). **B,** ROS levels in the brain of young (left histograms) GFAP IR KO mice are significantly increased as compared to controls while old GFAP IR KO mice show slightly reduced levels (n=). **C,** The MAG/PLP1 ratio is not altered in young GFAP IR KO mice (control 8, and tamoxifen 5). **D-E,** Expression of angiogenic mediators MmP14 (D) and PTGS1 (E) is not altered in the brain of young GFAP IR KO mice (n=).

Supplementary Figure 4: A-G, Brain mRNA levels of VEGFa (A), VEGFc (B), TGFβ3 (C), ErbB2 (D), vWF (E), Mmp14 (F), and PTGS1 (G) are significantly increased in GLAST IR KO mice as compared to control (vehicle-injected) littermates (n=7 per group; *p<0.05; **p<0.01 and ***p<0.0001).

Supplementary Figure 5: A, Insulin increases VEGF/HIF1α levels in wild type astrocytes (n= ; t-test, t= ; **p<0.01). **B,** IR levels are reduced in shIR-treated astrocytes (n= ; t-test, t= ; **p<0.01).

Supplementary Figure 6: **A** Mitochondrial depolarization was determined by JC1 staining and flow cytometry. Upper plots: representative red versus green fluorescence scatter in siRNA scramble (left) and siRNA IR (right) nucleofected cells. Lower: representative histograms of cell counts and their red (left) or green JC1 fluorescence (right) intensity levels in siRNA scramble (grey line) and siRNA IR nucleofected astrocytes (black line). **B-E,** Cyclosporine treatment of shIR astrocytes normalized the Mfn2/Fis1 ratio (B), and the levels of HIF1α (C), VEGF (D) and GluT1 (E) (n=).

Supplementary Figure 7: A, Anxiety levels, as determined by increased time in the open arms of the elevated plus maze, are decreased in young (left histograms) in GFAP

IR KO mice (n= , t-test, t= ; *p<0.05), whereas in adult mice anxiety levels return to normal (right histograms). **B,** Adult (right histograms), but not young (left histograms) GFAP IR KO mice show increased immobilization time in the tail suspension test, an indicator of a depressive-like behavior and reduced resilience to stress (n= ; t-test, t= ; **p<0.01. **C,** In the forced swim test adult (right histograms), but not young (left histograms) GFAP IR KO mice show increased depressive-like performance, with less time spent swimming (n= ; t-test, t= ; *p<0.05). **D,** Performance in the Y maze, a measure of working memory, was similar in both young (left histograms) and adult (right histograms) GFAP IR KO mice and controls. **E,** Both young (upper histograms) and adult (lower histograms) performed similarly in the Barnes maze as compared to respective littermates, indicating intact spatial learning (n= 6/group in all tests).

References

Abbott, N.J., Ronnback, L., and Hansson, E. (2006). Astrocyte-endothelial interactions at the blood-brain barrier. Nat Rev Neurosci *7*, 41-53. 10.1038/nrn1824.
Abu-Judeh, H.H., Levine, S., Kumar, M., el-Zeftawy, H., Naddaf, S., Lou, J.Q., and Abdel-Dayem, H.M. (1998). Comparison of SPET brain perfusion and 18F-FDG brain metabolism in patients with chronic fatigue syndrome. Nucl Med Commun *19*, 1065-1071.
Agarwal, A., Wu, P.H., Hughes, E.G., Fukaya, M., Tischfield, M.A., Langseth, A.J., Wirtz, D., and Bergles, D.E. (2017). Transient Opening of the Mitochondrial Permeability Transition Pore Induces Microdomain Calcium Transients in Astrocyte Processes. Neuron *93*, 587-605.e587. 10.1016/j.neuron.2016.12.034.
Angelova, P.R., Kasymov, V., Christie, I., Sheikhbahaei, S., Turovsky, E., Marina, N., Korsak, A., Zwicker, J., Teschemacher, A.G., Ackland, G.L., et al. (2015). Functional Oxygen Sensitivity of Astrocytes. J Neurosci *35*, 10460-10473. 10.1523/JNEUROSCI.0045-15.2015.
Apostolova, I., Wunder, A., Dirnagl, U., Michel, R., Stemmer, N., Lukas, M., Derlin, T., Gregor-Mamoudou, B., Goldschmidt, J., Brenner, W., and Buchert, R. (2012). Brain perfusion SPECT in the mouse: normal pattern according to gender and age. Neuroimage *63*, 1807-1817. 10.1016/j.neuroimage.2012.08.038.
Banks, W.A., Jaspan, J.B., Huang, W., and Kastin, A.J. (1997). Transport of insulin across the blood-brain barrier: saturability at euglycemic doses of insulin. Peptides *18*, 1423-1429.
Barker, R., Ashby, E.L., Wellington, D., Barrow, V.M., Palmer, J.C., Kehoe, P.G., Esiri, M.M., and Love, S. (2014). Pathophysiology of white matter perfusion in Alzheimer's disease and vascular dementia. Brain *137*, 1524-1532. 10.1093/brain/awu040.
Baron-Van, E.A., Olichon-Berthe, C., Kowalski, A., Visciano, G., and Van, O.E. (1991). Expression of IGF-I and insulin receptor genes in the rat central nervous system: a developmental, regional, and cellular analysis. J. Neurosci Res *28*, 244-253.
Baskin, D.G., Brewitt, B., Davidson, D.A., Corp, E., Paquette, T., Figlewicz, D.P., Lewellen, T.K., Graham, M.K., Woods, S.G., and Dorsa, D.M. (1986). Quantitative autoradiographic evidence for insulin receptors in the choroid plexus of the rat brain. Diabetes *35*, 246-249.
Behrens, M.M., Ali, S.S., Dao, D.N., Lucero, J., Shekhtman, G., Quick, K.L., and Dugan, L.L. (2007). Ketamine-induced loss of phenotype of fast-spiking interneurons is mediated by NADPH-oxidase. Science *318*, 1645-1647. 10.1126/science.1148045.
Cai, W., Xue, C., Sakaguchi, M., Konishi, M., Shirazian, A., Ferris, H.A., Li, M.E., Yu, R., Kleinridders, A., Pothos, E.N., and Kahn, C.R. (2018). Insulin regulates astrocyte gliotransmission and modulates behavior. The Journal of Clinical Investigation *128*, 2914-2926. 10.1172/JCI99366.
Chang, J., Jung, H.J., Jeong, S.H., Kim, H.K., Han, J., and Kwon, H.J. (2014). A mutation in the mitochondrial protein UQCRB promotes angiogenesis through the generation of mitochondrial reactive oxygen species. Biochem Biophys Res Commun *455*, 290-297. 10.1016/j.bbrc.2014.11.005.
Citron, M., Westaway, D., Xia, W., Carlson, G., Diehl, T., Levesque, G., Johnson-Wood, K., Lee, M., Seubert, P., Davis, A., et al. (1997). Mutant presenilins of Alzheimer's disease increase production of 42-residue amyloid ?-protein in both transfected cells and transgenic mice. Nature Medicine *3*, 67-72.

Cohen-Salmon, M., Slaoui, L., Mazare, N., Gilbert, A., Oudart, M., Alvear-Perez, R., Elorza-Vidal, X., Chever, O., and Boulay, A.C. (2021). Astrocytes in the regulation of cerebrovascular functions. Glia *69*, 817-841. 10.1002/glia.23924.
Cohen, S., Liu, Q., Wright, M., Garvin, J., Rarick, K., and Harder, D. (2019). High glucose conditioned neonatal astrocytes results in impaired mitogenic activity in cerebral microvessel endothelial cells in co-culture. Heliyon *5*, e01795. 10.1016/j.heliyon.2019.e01795.
Das, A., Huang, G.X., Bonkowski, M.S., Longchamp, A., Li, C., Schultz, M.B., Kim, L.-J., Osborne, B., Joshi, S., Lu, Y., et al. (2018). Impairment of an Endothelial NAD⁺-H₂S Signaling Network Is a Reversible Cause of Vascular Aging. Cell *173*, 74-89.e20. 10.1016/j.cell.2018.02.008.
Devor, A., Hillman, E.M., Tian, P., Waeber, C., Teng, I.C., Ruvinskaya, L., Shalinsky, M.H., Zhu, H., Haslinger, R.H., Narayanan, S.N., et al. (2008). Stimulus-induced changes in blood flow and 2-deoxyglucose uptake dissociate in ipsilateral somatosensory cortex. J Neurosci *28*, 14347-14357. 10.1523/jneurosci.4307-08.2008.
Devous, M.D., Sr. (2002). Functional brain imaging in the dementias: role in early detection, differential diagnosis, and longitudinal studies. Eur J Nucl Med Mol Imaging *29*, 1685-1696. 10.1007/s00259-002-0967-2.
Elmore, S.P., Qian, T., Grissom, S.F., and Lemasters, J.J. (2001). The mitochondrial permeability transition initiates autophagy in rat hepatocytes. FASEB J *15*, 2286-2287. 10.1096/fj.01-0206fje.
Esteban-Martinez, L., Sierra-Filardi, E., McGreal, R.S., Salazar-Roa, M., Marino, G., Seco, E., Durand, S., Enot, D., Grana, O., Malumbres, M., et al. (2017). Programmed mitophagy is essential for the glycolytic switch during cell differentiation. EMBO J *36*, 1688-1706. 10.15252/embj.201695916.
Fernandez, A.M., Fernandez, S., Carrero, P., Garcia-Garcia, M., and Torres-Aleman, I. (2007). Calcineurin in reactive astrocytes plays a key role in the interplay between proinflammatory and anti-inflammatory signals. J Neurosci *27*, 8745-8756.
Fernandez, A.M., Hernandez-Garzon, E., Perez-Domper, P., Perez-Alvarez, A., Mederos, S., Matsui, T., Santi, A., Trueba-Saiz, A., Garcia-Guerra, L., Pose-Utrilla, J., et al. (2017). Insulin Regulates Astrocytic Glucose Handling Through Cooperation With IGF-I. Diabetes *66*, 64-74. 10.2337/db16-0861.
Fernandez, A.M., Jimenez, S., Mecha, M., Davila, D., Guaza, C., Vitorica, J., and Torres-Aleman, I. (2012). Regulation of the phosphatase calcineurin by insulin-like growth factor I unveils a key role of astrocytes in Alzheimer's pathology. Mol Psychiatry *17*, 705-718.
Fernandez, A.M., and Torres-Aleman, I. (2012). The many faces of insulin-like peptide signalling in the brain. Nat Rev Neurosci *13*, 225-239.
Filippini, N., Ebmeier, K.P., MacIntosh, B.J., Trachtenberg, A.J., Frisoni, G.B., Wilcock, G.K., Beckmann, C.F., Smith, S.M., Matthews, P.M., and Mackay, C.E. (2011). Differential effects of the APOE genotype on brain function across the lifespan. Neuroimage *54*, 602-610. 10.1016/j.neuroimage.2010.08.009.
Fisher, J.P., Hartwich, D., Seifert, T., Olesen, N.D., McNulty, C.L., Nielsen, H.B., van Lieshout, J.J., and Secher, N.H. (2013). Cerebral perfusion, oxygenation and metabolism during exercise in young and elderly individuals. J Physiol *591*, 1859-1870. 10.1113/jphysiol.2012.244905.
Fraisl, P., Mazzone, M., Schmidt, T., and Carmeliet, P. (2009). Regulation of angiogenesis by oxygen and metabolism. Dev Cell *16*, 167-179. 10.1016/j.devcel.2009.01.003.

Frank, H.J., Pardridge, W.M., Morris, W.L., Rosenfeld, R.G., and Choi, T.B. (1986). Binding and internalization of insulin and insulin-like growth factors by isolated brain microvessels. Diabetes *35*, 654-661.
Friesen, M., Hudak, C.S., Warren, C.R., Xia, F., and Cowan, C.A. (2016). Adipocyte insulin receptor activity maintains adipose tissue mass and lifespan. Biochem Biophys Res Commun *476*, 487-492. 10.1016/j.bbrc.2016.05.151.
Ganat, Y.M., Silbereis, J., Cave, C., Ngu, H., Anderson, G.M., Ohkubo, Y., Ment, L.R., and Vaccarino, F.M. (2006). Early postnatal astroglial cells produce multilineage precursors and neural stem cells in vivo. J Neurosci *26*, 8609-8621. 10.1523/JNEUROSCI.2532-06.2006.
Garcia-Caceres, C., Quarta, C., Varela, L., Gao, Y., Gruber, T., Legutko, B., Jastroch, M., Johansson, P., Ninkovic, J., Yi, C.X., et al. (2016). Astrocytic Insulin Signaling Couples Brain Glucose Uptake with Nutrient Availability. Cell *166*, 867-880. 10.1016/j.cell.2016.07.028.
Garcia-Segura, L.M., Rodriguez, J.R., and Torres-Aleman, I. (1997). Localization of the insulin-like growth factor I receptor in the cerebellum and hypothalamus of adult rats: an electron microscopic study. J Neurocytol *26*, 479-490.
Gbel, J., Engelhardt, E., Pelzer, P., Sakthivelu, V., Jahn, H.M., Jevtic, M., Folz-Donahue, K., Kukat, C., Schauss, A., Frese, C.K., et al. (2020). Mitochondria-Endoplasmic Reticulum Contacts in Reactive Astrocytes Promote Vascular Remodeling. Cell Metab *31*, 791-808 e798. 10.1016/j.cmet.2020.03.005.
Gomez-Arboledas, A., Davila, J.C., Sanchez-Mejias, E., Navarro, V., Nunez-Diaz, C., Sanchez-Varo, R., Sanchez-Mico, M.V., Trujillo-Estrada, L., Fernandez-Valenzuela, J.J., Vizuete, M., et al. (2018). Phagocytic clearance of presynaptic dystrophies by reactive astrocytes in Alzheimer's disease. Glia *66*, 637-653. 10.1002/glia.23270.
Gray, S.M., Aylor, K.W., and Barrett, E.J. (2017). Unravelling the regulation of insulin transport across the brain endothelial cell. Diabetologia *60*, 1512-1521. 10.1007/s00125-017-4285-4.
Gray, S.M., Meijer, R.I., and Barrett, E.J. (2014). Insulin regulates brain function, but how does it get there?
2. Diabetes *63*, 3992-3997.
Hamanaka, R.B., and Chandel, N.S. (2009). Mitochondrial reactive oxygen species regulate hypoxic signaling. Curr Opin Cell Biol *21*, 894-899. 10.1016/j.ceb.2009.08.005.
Hernandez-Garzon, E., Fernandez, A.M., Perez-Alvarez, A., Genis, L., Bascunana, P., Fernandez de la Rosa, R., Delgado, M., Angel Pozo, M., Moreno, E., McCormick, P.J., et al. (2016). The insulin-like growth factor I receptor regulates glucose transport by astrocytes. Glia *64*, 1962-1971. 10.1002/glia.23035.
Hersom, M., Helms, H.C., Schmalz, C., Pedersen, T.A., Buckley, S.T., and Brodin, B. (2018). The insulin receptor is expressed and functional in cultured blood-brain barrier endothelial cells, but does not mediate insulin entry from blood-to-brain. Am J Physiol Endocrinol Metab *315*, 531-542. 10.1152/ajpendo.00350.2016.
Iadecola, C. (2017). The Neurovascular Unit Coming of Age: A Journey through Neurovascular Coupling in Health and Disease. Neuron *96*, 17-42. 10.1016/j.neuron.2017.07.030.
Iturria-Medina, Y., Sotero, R.C., Toussaint, P.J., Mateos-Perez, J.M., Evans, A.C., and Alzheimer's Disease Neuroimaging, I. (2016). Early role of vascular dysregulation on late-onset Alzheimer's disease based on multifactorial data-driven analysis. Nat Commun *7*, 11934. 10.1038/ncomms11934.

Jacquier-Sarlin, M.R., Polla, B.S., and Slosman, D.O. (1996). Oxido-reductive state: the major determinant for cellular retention of technetium-99m-HMPAO. J Nucl Med *37*, 1413-1416.
Jais, A., Solas, M., Backes, H., Chaurasia, B., Kleinridders, A., Theurich, S., Mauer, J., Steculorum, S.M., Hampel, B., Goldau, J., et al. (2016). Myeloid-Cell-Derived VEGF Maintains Brain Glucose Uptake and Limits Cognitive Impairment in Obesity. Cell *165*, 882-895. 10.1016/j.cell.2016.03.033.
Kacem, K., Lacombe, P., Seylaz, J., and Bonvento, G. (1998). Structural organization of the perivascular astrocyte endfeet and their relationship with the endothelial glucose transporter: a confocal microscopy study. Glia *23*, 1-10.
King, G.L., and Johnson, S.M. (1985). Receptor-mediated transport of insulin across endothelial cells. Science *227*, 1583-1586.
Koehler, R.C., Roman, R.J., and Harder, D.R. (2009). Astrocytes and the regulation of cerebral blood flow. Trends Neurosci *32*, 160-169. 10.1016/j.tins.2008.11.005.
Konishi, M., Sakaguchi, M., Lockhart, S.M., Cai, W., Li, M.E., Homan, E.P., Rask-Madsen, C., and Kahn, C.R. (2017). Endothelial insulin receptors differentially control insulin signaling kinetics in peripheral tissues and brain of mice. Proc Natl Acad Sci U S A *114*, E8478-E8487. 10.1073/pnas.1710625114.
Kuntner, C., Kesner, A.L., Bauer, M., Kremslehner, R., Wanek, T., Mandler, M., Karch, R., Stanek, J., Wolf, T., Muller, M., and Langer, O. (2009). Limitations of small animal PET imaging with [18F]FDDNP and FDG for quantitative studies in a transgenic mouse model of Alzheimer's disease. Mol Imaging Biol *11*, 236-240. 10.1007/s11307-009-0198-z.
Kuwabara, T.K. (2011). Insulin biosynthesis in neuronal progenitors derived from adult hippocampus and the olfactory bulb
805. EMBO Molecular Medicine *3*, 742-754. 10.1002/emmm.201100177.
Leão, L.L., Tangen, G., Barca, M.L., Engedal, K., Santos, S.H.S., Machado, F.S.M., de Paula, A.M.B., and Monteiro-Junior, R.S. (2020). Does hyperglycemia downregulate glucose transporters in the brain? Med Hypotheses *139*, 109614. 10.1016/j.mehy.2020.109614.
Leuzy, A., Rodriguez-Vieitez, E., Saint-Aubert, L., Chiotis, K., Almkvist, O., Savitcheva, I., Jonasson, M., Lubberink, M., Wall, A., Antoni, G., and Nordberg, A. (2018). Longitudinal uncoupling of cerebral perfusion, glucose metabolism, and tau deposition in Alzheimer's disease. Alzheimer's & dementia : the journal of the Alzheimer's Association *14*, 652-663. 10.1016/j.jalz.2017.11.008.
Ma, Z., Stork, T., Bergles, D.E., and Freeman, M.R. (2016). Neuromodulators signal through astrocytes to alter neural circuit activity and behaviour. Nature *539*, 428-432. 10.1038/nature20145.
Manaserh, I.H., Chikkamenahalli, L., Ravi, S., Dube, P.R., Park, J.J., and Hill, J.W. (2019). Ablating astrocyte insulin receptors leads to delayed puberty and hypogonadism in mice. PLoS Biol *17*, e3000189. 10.1371/journal.pbio.3000189.
Marcu, R., Zheng, Y., and Hawkins, B.J. (2017). Mitochondria and Angiogenesis. Adv Exp Med Biol *982*, 371-406. 10.1007/978-3-319-55330-6_21.
Margolis, R.U., and Altszuler, N. (1967). Insulin in the cerebrospinal fluid. Nature *215*, 1375-1376.
Marina, N., Turovsky, E., Christie, I.N., Hosford, P.S., Hadjihambi, A., Korsak, A., Ang, R., Mastitskaya, S., Sheikhbahaei, S., Theparambil, S.M., and Gourine, A.V. (2018). Brain metabolic sensing and metabolic signaling at the level of an astrocyte. Glia *66*, 1185-1199. doi:10.1002/glia.23283.

Martinez-Rachadell, L., Aguilera, A., Perez-Domper, P., Pignatelli, J., Fernandez, A.M., and Torres-Aleman, I. (2019). Cell-specific expression of insulin/insulin-like growth factor-I receptor hybrids in the mouse brain. Growth Horm IGF Res *45*, 25-30. 10.1016/j.ghir.2019.02.003.
Mathiisen, T.M., Lehre, K.P., Danbolt, N.C., and Ottersen, O.P. (2010). The perivascular astroglial sheath provides a complete covering of the brain microvessels: an electron microscopic 3D reconstruction. Glia *58*, 1094-1103. 10.1002/glia.20990.
Maulucci, G., Bacic, G., Bridal, L., Schmidt, H.H., Tavitian, B., Viel, T., Utsumi, H., Yalcin, A.S., and De Spirito, M. (2016a). Imaging Reactive Oxygen Species-Induced Modifications in Living Systems. Antioxid Redox Signal *24*, 939-958. 10.1089/ars.2015.6415.
Maulucci, G., Bačić, G., Bridal, L., Schmidt, H.H., Tavitian, B., Viel, T., Utsumi, H., Yalçın, A.S., and De Spirito, M. (2016b). Imaging Reactive Oxygen Species-Induced Modifications in Living Systems. Antioxidants & redox signaling *24*, 939-958. 10.1089/ars.2015.6415.
Moulton, C.D., Pickup, J.C., and Ismail, K. (2015). The link between depression and diabetes: the search for shared mechanisms. Lancet Diabetes Endocrinol *3*, 461-471. 10.1016/S2213-8587(15)00134-5.
Munive, V., Zegarra-Valdivia, J.A., Herrero-Labrador, R., Fernandez, A.M., and Aleman, I.T. (2019). Loss of the interaction between estradiol and insulin-like growth factor I in brain endothelial cells associates to changes in mood homeostasis during peri-menopause in mice. Aging (Albany NY) *11*, 174-184. 10.18632/aging.101739.
Muniyappa, R., and Sowers, J.R. (2013). Role of insulin resistance in endothelial dysfunction. Rev Endocr Metab Disord *14*, 5-12. 10.1007/s11154-012-9229-1.
Novak, V., Milberg, W., Hao, Y., Munshi, M., Novak, P., Galica, A., Manor, B., Roberson, P., Craft, S., and Abduljalil, A. (2014). Enhancement of vasoreactivity and cognition by intranasal insulin in type 2 diabetes. Diabetes Care *37*, 751-759. 10.2337/dc13-1672.
Palikaras, K., Lionaki, E., and Tavernarakis, N. (2015). Coordination of mitophagy and mitochondrial biogenesis during ageing in C. elegans. Nature *521*, 525-528. 10.1038/nature14300.
Pansky, B., and Hatfield, J.S. (1978). Cerebral localization of insulin by immunofluorescence. Am J Anat *153*, 459-467. 10.1002/aja.1001530309.
Perriere, N., Demeuse, P., Garcia, E., Regina, A., Debray, M., Andreux, J.P., Couvreur, P., Scherrmann, J.M., Temsamani, J., Couraud, P.O., et al. (2005). Puromycin-based purification of rat brain capillary endothelial cell cultures. Effect on the expression of blood-brain barrier-specific properties
2. J Neurochem *93*, 279-289.
Polavarapu, R., Gongora, M.C., Winkles, J.A., and Yepes, M. (2005). Tumor Necrosis Factor-Like Weak Inducer of Apoptosis Increases the Permeability of the Neurovascular Unit through Nuclear Factor-{kappa}B Pathway Activation. Journal of Neuroscience *25*, 10094-10100.
Rasgon, N.L., and Kenna, H.A. (2005). Insulin resistance in depressive disorders and Alzheimer's disease: revisiting the missing link hypothesis. Neurobiol Aging *26 Suppl 1*, 103-107. 10.1016/j.neurobiolaging.2005.09.004.
Reichard, A., and Asosingh, K. (2019). The role of mitochondria in angiogenesis. Mol Biol Rep *46*, 1393-1400. 10.1007/s11033-018-4488-x.
Rhea, E.M., Rask-Madsen, C., and Banks, W.A. (2018). Insulin transport across the blood–brain barrier can occur independently of the insulin receptor. The Journal of Physiology *596*, 4753-4765. doi:10.1113/JP276149.

Roy, C.S., and Sherrington, C. (1890). On the regulation of the blood supply of the brain. J. Physiol *11*, 85-108.
Ruitenberg, A., den Heijer, T., Bakker, S.L., van Swieten, J.C., Koudstaal, P.J., Hofman, A., and Breteler, M.M. (2005). Cerebral hypoperfusion and clinical onset of dementia: the Rotterdam Study. Ann Neurol *57*, 789-794. 10.1002/ana.20493.
Rusinek, H., Ha, J., Yau, P.L., Storey, P., Tirsi, A., Tsui, W.H., Frosch, O., Azova, S., and Convit, A. (2015). Cerebral perfusion in insulin resistance and type 2 diabetes. J Cereb Blood Flow Metab *35*, 95-102. 10.1038/jcbfm.2014.173.
Sartorius, T., Peter, A., Heni, M., Maetzler, W., Fritsche, A., Haring, H.U., and Hennige, A.M. (2015). The brain response to peripheral insulin declines with age: a contribution of the blood-brain barrier?
1. PLoS ONE *10*, e0126804.
Schwartz, M.W., and Porte, D. (2005). Diabetes, obesity, and the brain. Science *307*, 375-379.
Simionescu, M., Gafencu, A., and Antohe, F. (2002). Transcytosis of plasma macromolecules in endothelial cells: A cell biological survey. Microsc. Res. Tech *57*, 269-288.
Stoltzman, C.A., Peterson, C.W., Breen, K.T., Muoio, D.M., Billin, A.N., and Ayer, D.E. (2008). Glucose sensing by MondoA:Mlx complexes: a role for hexokinases and direct regulation of thioredoxin-interacting protein expression. Proc Natl Acad Sci U S A *105*, 6912-6917. 10.1073/pnas.0712199105.
Szabadkai, G., Bianchi, K., Várnai, P., De Stefani, D., Wieckowski, M.R., Cavagna, D., Nagy, A.I., Balla, T., and Rizzuto, R. (2006). Chaperone-mediated coupling of endoplasmic reticulum and mitochondrial Ca2+ channels. J Cell Biol *175*, 901-911. 10.1083/jcb.200608073.
Takahashi, N., Kuwaki, T., Kiyonaka, S., Numata, T., Kozai, D., Mizuno, Y., Yamamoto, S., Naito, S., Knevels, E., Carmeliet, P., et al. (2011). TRPA1 underlies a sensing mechanism for O2. Nat Chem Biol *7*, 701-711. 10.1038/nchembio.640.
Talbot, K., Wang, H.Y., Kazi, H., Han, L.Y., Bakshi, K.P., Stucky, A., Fuino, R.L., Kawaguchi, K.R., Samoyedny, A.J., Wilson, R.S., et al. (2012). Demonstrated brain insulin resistance in Alzheimer's disease patients is associated with IGF-1 resistance, IRS-1 dysregulation, and cognitive decline. J. Clin. Invest *122*, 1316-1338.
Thomas, T., Miners, S., and Love, S. (2015). Post-mortem assessment of hypoperfusion of cerebral cortex in Alzheimer's disease and vascular dementia. Brain *138*, 1059-1069. 10.1093/brain/awv025.
Tiefenbock, S.K., Baltzer, C., Egli, N.A., and Frei, C. (2010). The Drosophila PGC-1 homologue Spargel coordinates mitochondrial activity to insulin signalling. EMBO J *29*, 171-183. 10.1038/emboj.2009.330.
Toth, P., Tarantini, S., Csiszar, A., and Ungvari, Z. (2017). Functional vascular contributions to cognitive impairment and dementia: mechanisms and consequences of cerebral autoregulatory dysfunction, endothelial impairment, and neurovascular uncoupling in aging. American journal of physiology. Heart and circulatory physiology *312*, H1-h20. 10.1152/ajpheart.00581.2016.
Tubbs, E., and Rieusset, J. (2016). Study of Endoplasmic Reticulum and Mitochondria Interactions by In Situ Proximity Ligation Assay in Fixed Cells. J Vis Exp. 10.3791/54899.
Twig, G., and Shirihai, O.S. (2011). The interplay between mitochondrial dynamics and mitophagy. Antioxidants & redox signaling *14*, 1939-1951. 10.1089/ars.2010.3779.
Ward, J.P. (2008). Oxygen sensors in context. Biochim Biophys Acta *1777*, 1-14. 10.1016/j.bbabio.2007.10.010.

Warmke, N., Platt, F., Bruns, A.F., Ozber, C.H., Haywood, N.J., Abudushalamu, Y., Slater, C., Palin, V., Sukumar, P., Wheatcroft, S.B., et al. (2021). Pericyte insulin receptors modulate retinal vascular remodeling and endothelial angiopoietin signaling. Endocrinology. 10.1210/endocr/bqab182.
Watson, K., Nasca, C., Aasly, L., McEwen, B., and Rasgon, N. (2018). Insulin resistance, an unmasked culprit in depressive disorders: Promises for interventions. Neuropharmacology *136*, 327-334. https://doi.org/10.1016/j.neuropharm.2017.11.038.
Wenz, T. (2013). Regulation of mitochondrial biogenesis and PGC-1alpha under cellular stress. Mitochondrion *13*, 134-142. 10.1016/j.mito.2013.01.006.
Willems, P.H., Rossignol, R., Dieteren, C.E., Murphy, M.P., and Koopman, W.J. (2015). Redox Homeostasis and Mitochondrial Dynamics. Cell Metab *22*, 207-218. 10.1016/j.cmet.2015.06.006.
Zerarka, S., Pellerin, L., Slosman, D., and Magistretti, P.J. (2001). Astrocytes as a predominant cellular site of (99m)Tc-HMPAO retention. J Cereb Blood Flow Metab *21*, 456-468. 10.1097/00004647-200104000-00014.
Zhao, N., Liu, C.C., Van Ingelgom, A.J., Martens, Y.A., Linares, C., Knight, J.A., Painter, M.M., Sullivan, P.M., and Bu, G. (2017). Apolipoprotein E4 Impairs Neuronal Insulin Signaling by Trapping Insulin Receptor in the Endosomes. Neuron *96*, 115-129 e115. 10.1016/j.neuron.2017.09.003.
Zheng, C., and Liu, Z. (2015). Vascular function, insulin action, and exercise: an intricate interplay. Trends Endocrinol Metab *26*, 297-304. 10.1016/j.tem.2015.02.002.
Zlokovic, B.V. (2008). The Blood-Brain Barrier in Health and Chronic Neurodegenerative Disorders. Neuron *57*, 178-201.

A

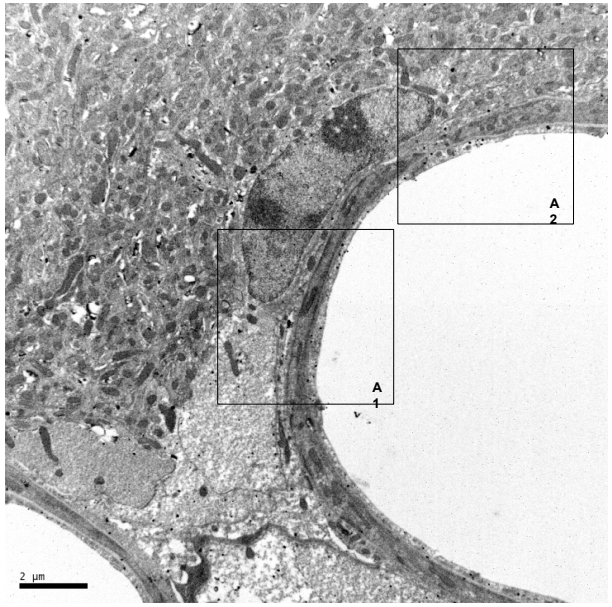

B

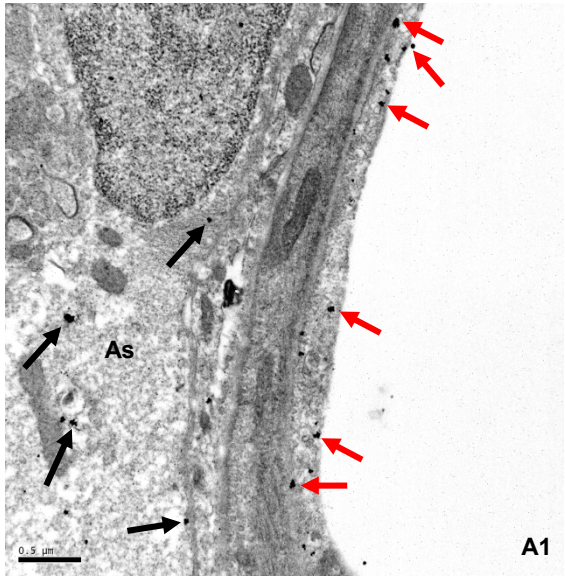

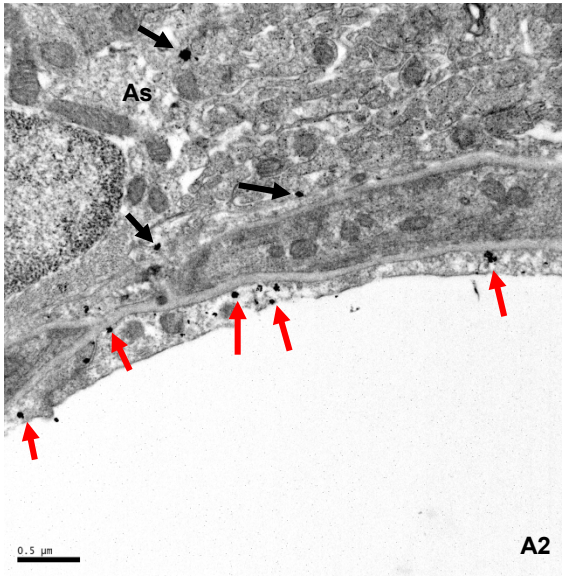

Figure 1

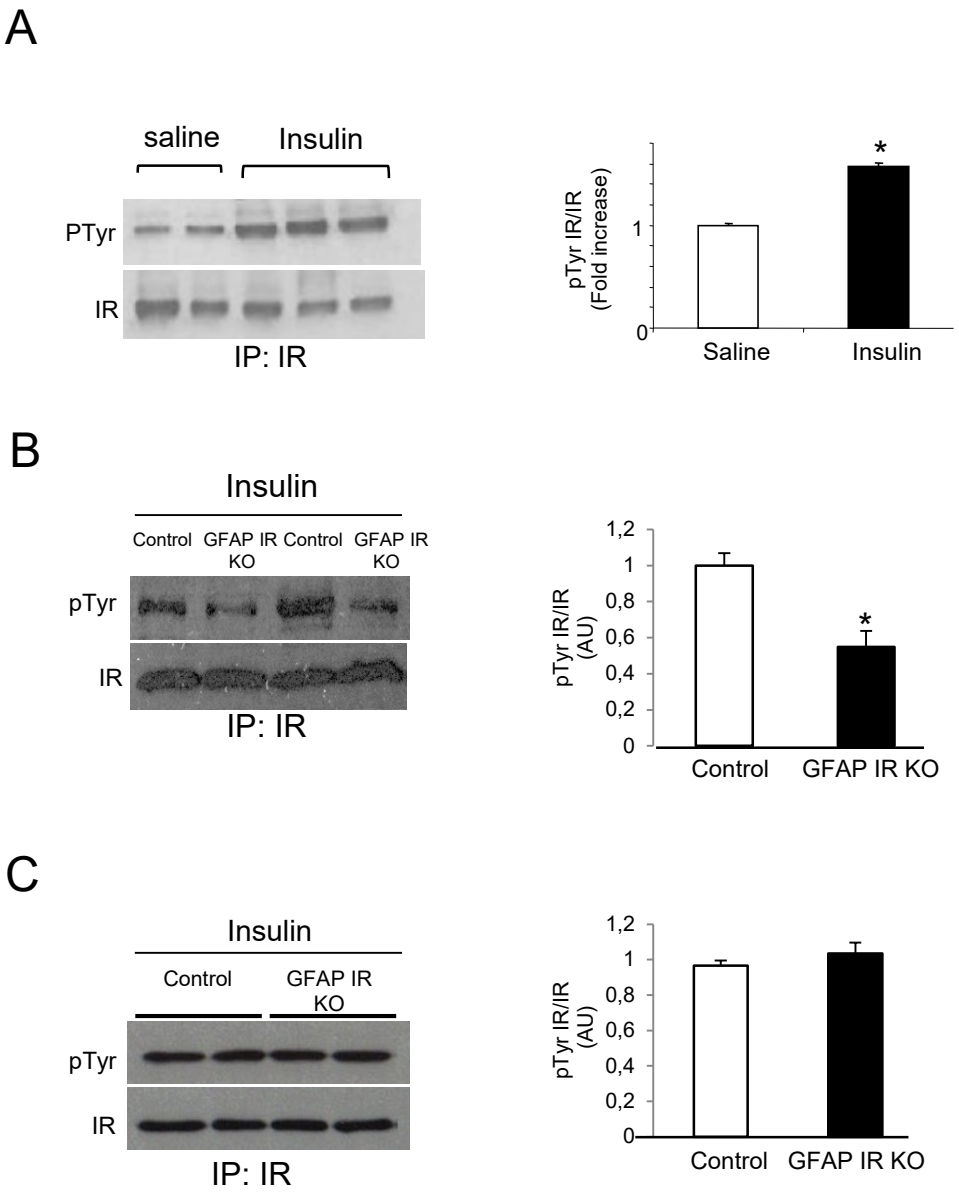
A
saline
Insulin
PTyr
IR
IP: IR
pTyr IR/IR
(Fold increase)
1
0
*
Saline
Insulin
B
Insulin
Control
GFAP IR KO
Control
GFAP IR KO
pTyr
IR
IP: IR
pTyr IR/IR
(AU)
1,2
1
0,8
0,6
0,4
0,2
0
*
Control
GFAP IR KO
C
Insulin
Control
GFAP IR KO
pTyr
IR
IP: IR
pTyr IR/IR
(AU)
1,2
1
0,8
0,6
0,4
0,2
0
Control
GFAP IR KO

Figure 2

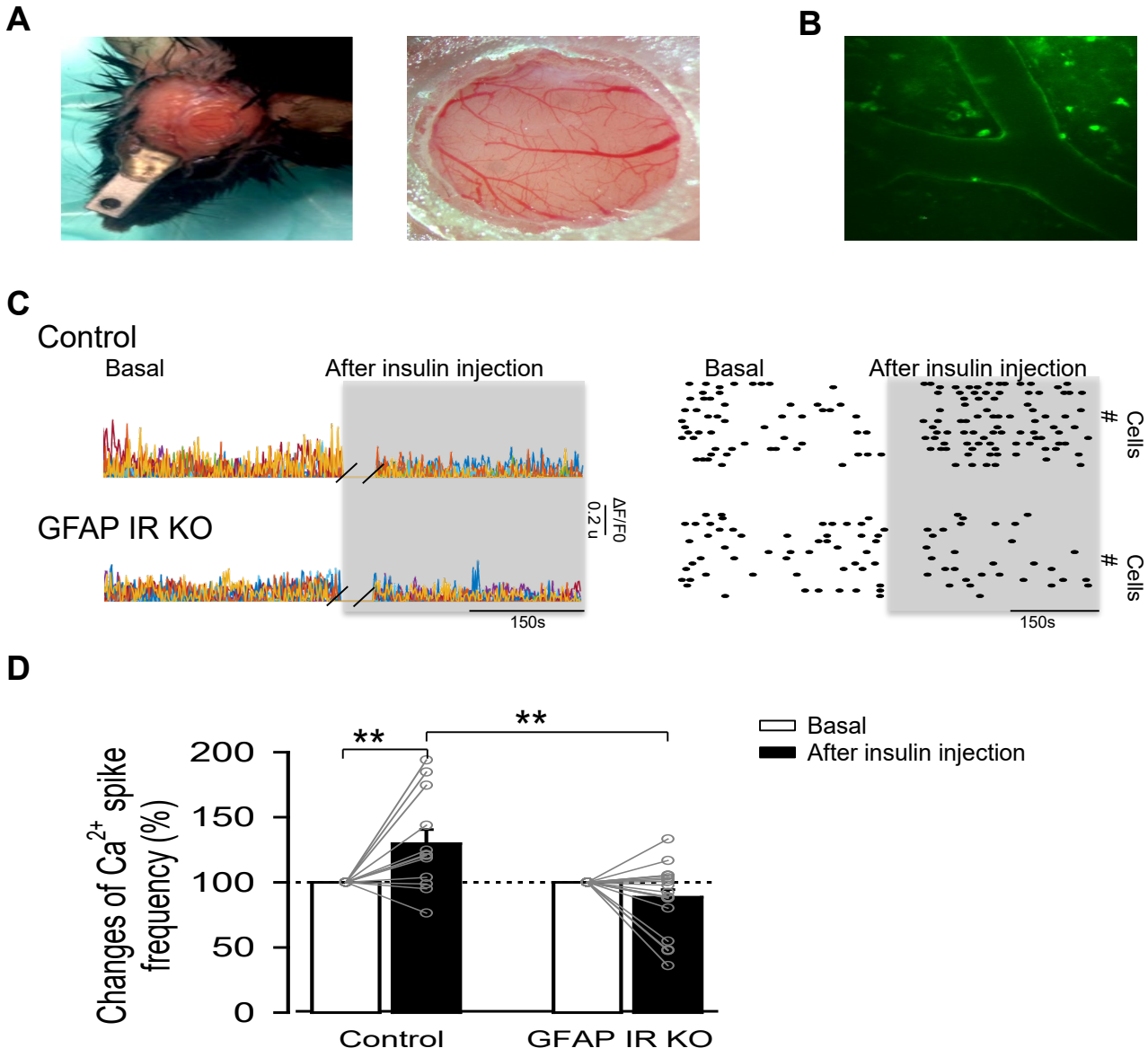
A
B
C
Control
Basal
After insulin injection
GFAP IR KO
ΔF/F0
0.2 u
150s
Basal
After insulin injection
Cells
Cells
150s
D
**
**
Basal
After insulin injection
Changes of Ca2+ spike frequency (%)
200
150
100
50
0
Control
GFAP IR KO

Figure 3

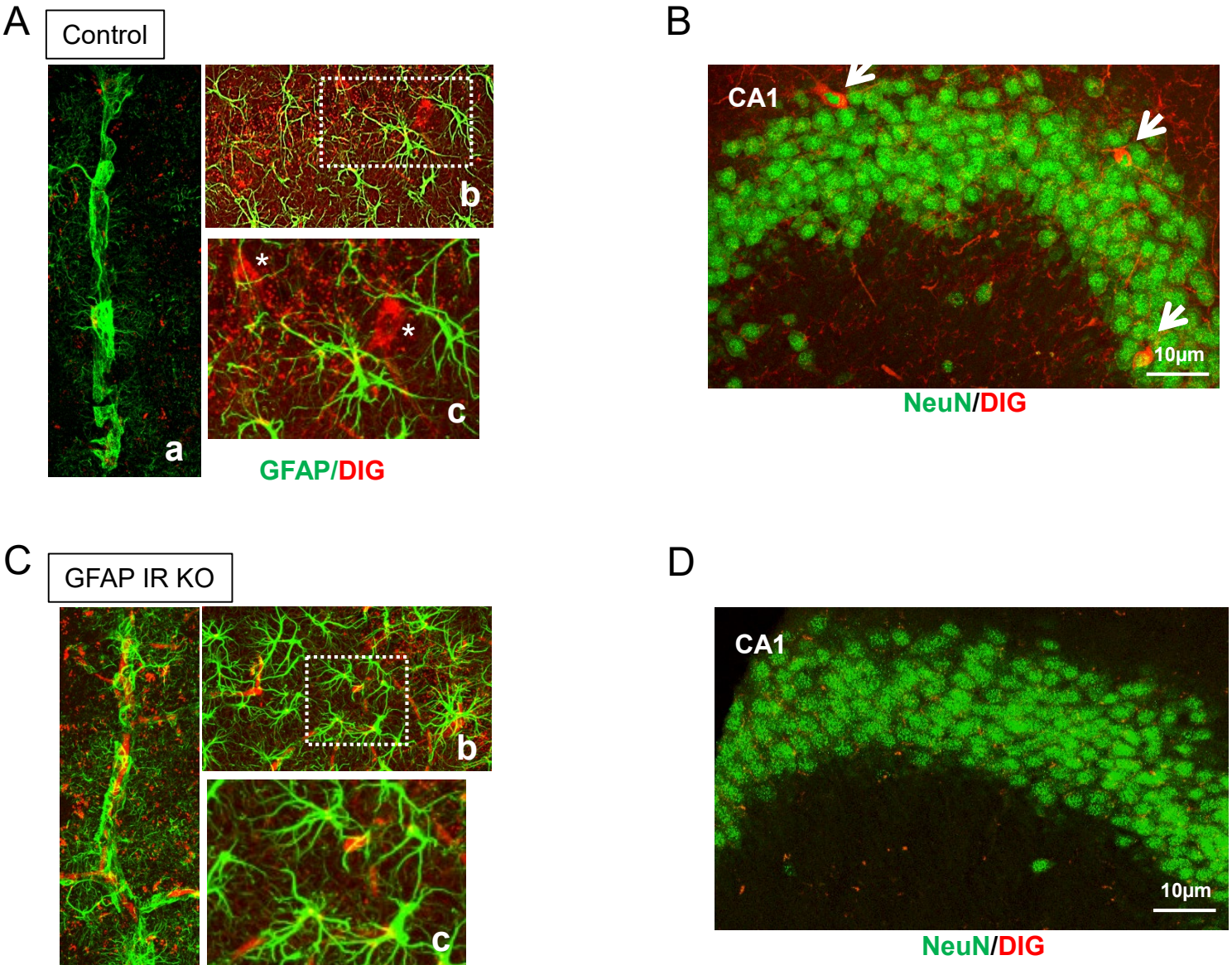
A
Control
a
b
c
*
*
GFAP/DIG
B
CA1
10μm
NeuN/DIG
C
GFAP IR KO
a
b
c
GFAP/DIG
D
CA1
10μm
NeuN/DIG

Figure 4

A

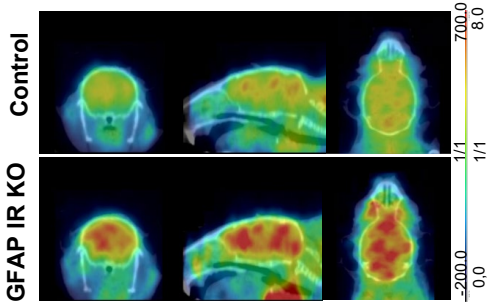
Control
GFAP IR KO
700,0
8,0
1/1
1/1
-200,0
0,0

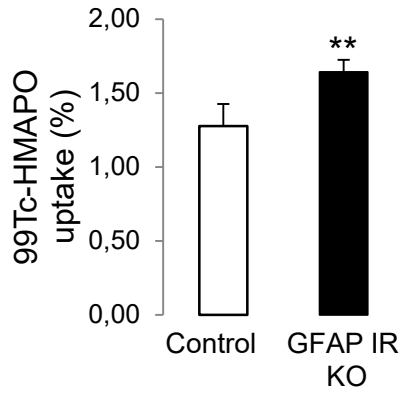
99Tc-HMAPO uptake (%)
2,00
1,50
1,00
0,50
0,00
**
Control
GFAP IR KO

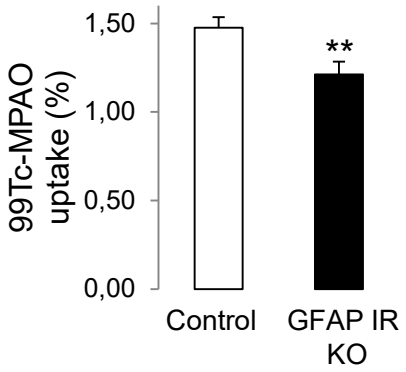
99Tc-MPAO uptake (%)
1,50
1,00
0,50
0,00
**
Control
GFAP IR KO

B

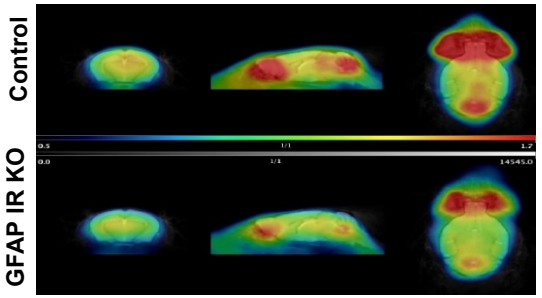
Control
GFAP IR KO

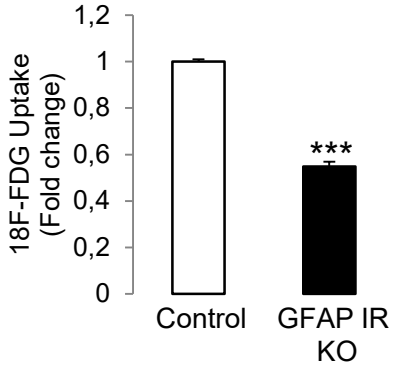
18F-FDG Uptake (Fold change)
1,2
1
0,8
0,6
0,4
0,2
0
***
Control
GFAP IR KO

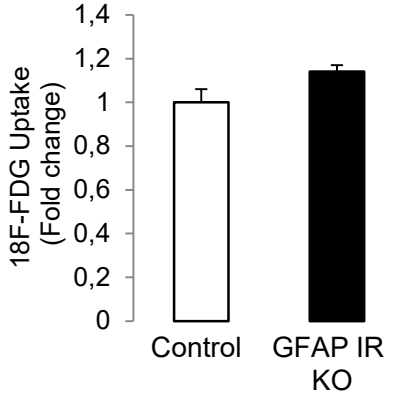
18F-FDG Uptake (Fold change)
1,4
1,2
1
0,8
0,6
0,4
0,2
0
Control
GFAP IR KO

Figure 5

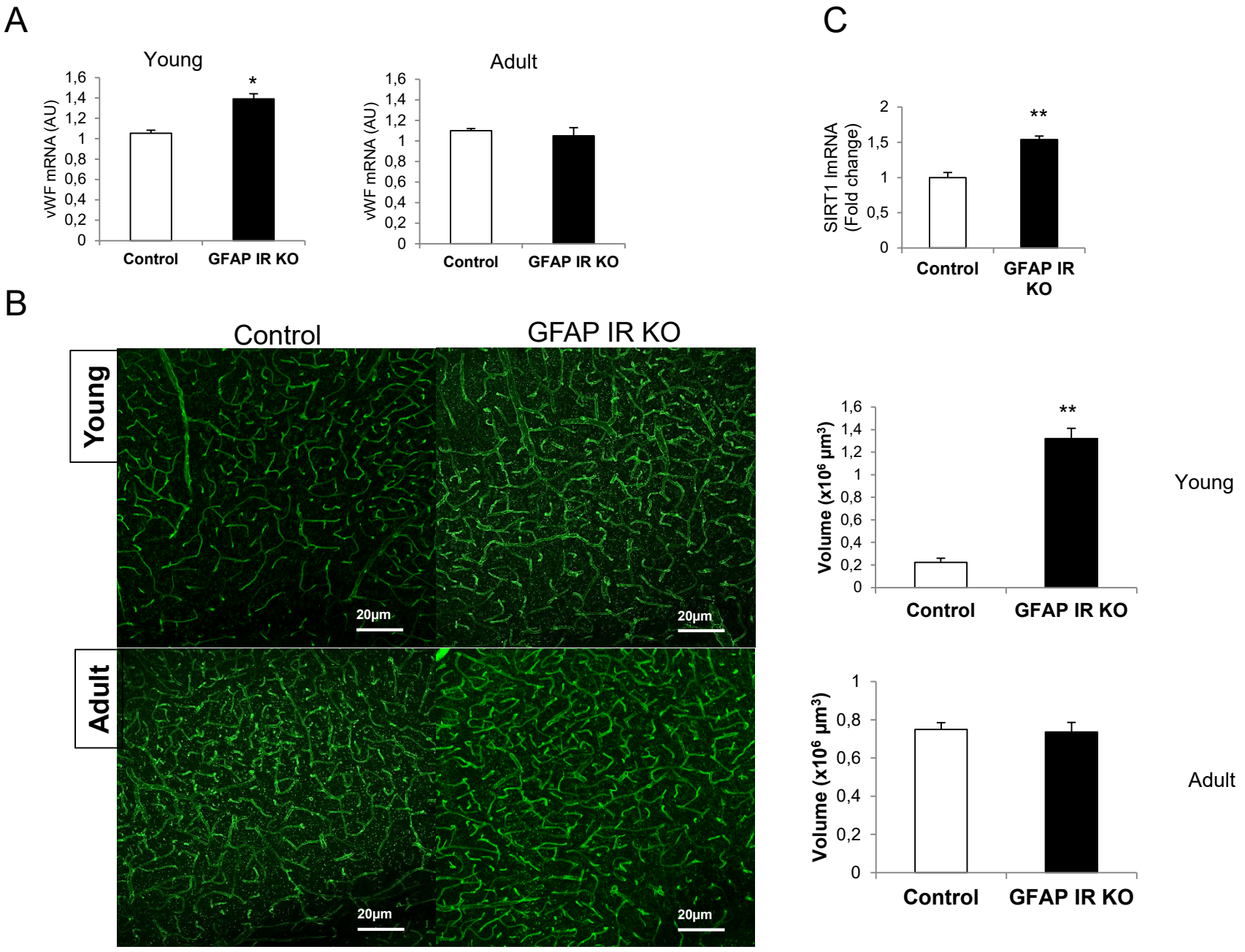
A
Young
Adult
vWF mRNA (AU)
1,6
1,4
1,2
1
0,8
0,6
0,4
0,2
0
*
Control
GFAP IR KO
C
SIRT1 ImRNA (Fold change)
2
1,5
1
0,5
0
**
Control
GFAP IR KO
B
Control
GFAP IR KO
Young
Adult
20µm
Volume (x10⁶ µm³)
**
Young
Adult
Control
GFAP IR KO

Figure 6

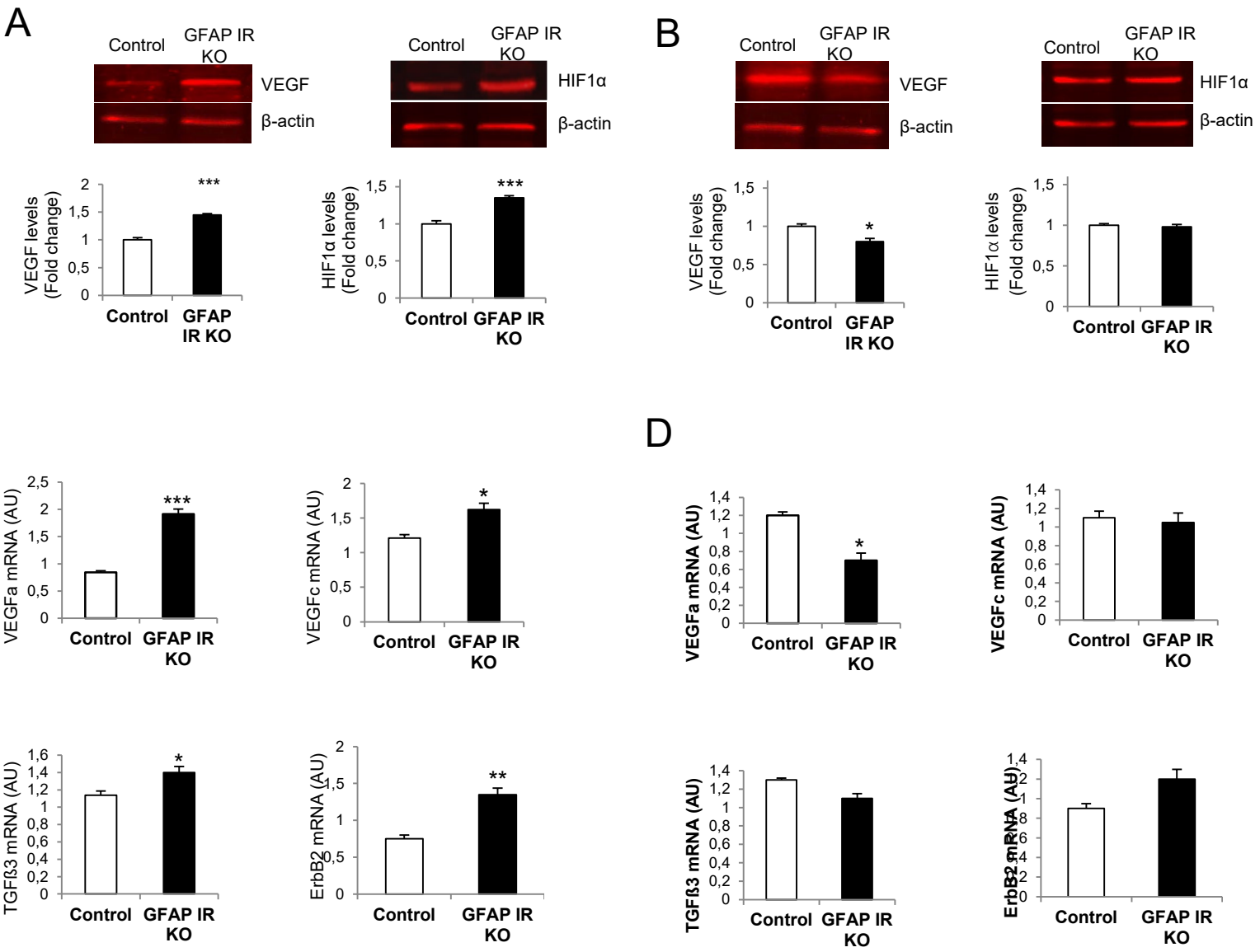
A
Control
GFAP IR KO
VEGF
β-actin
HIF1α
VEGF levels (Fold change)
HIF1α levels (Fold change)
***
B
*
C
VEGFa mRNA (AU)
VEGFc mRNA (AU)
TGFß3 mRNA (AU)
ErbB2 mRNA (AU)
**
D

Figure 7

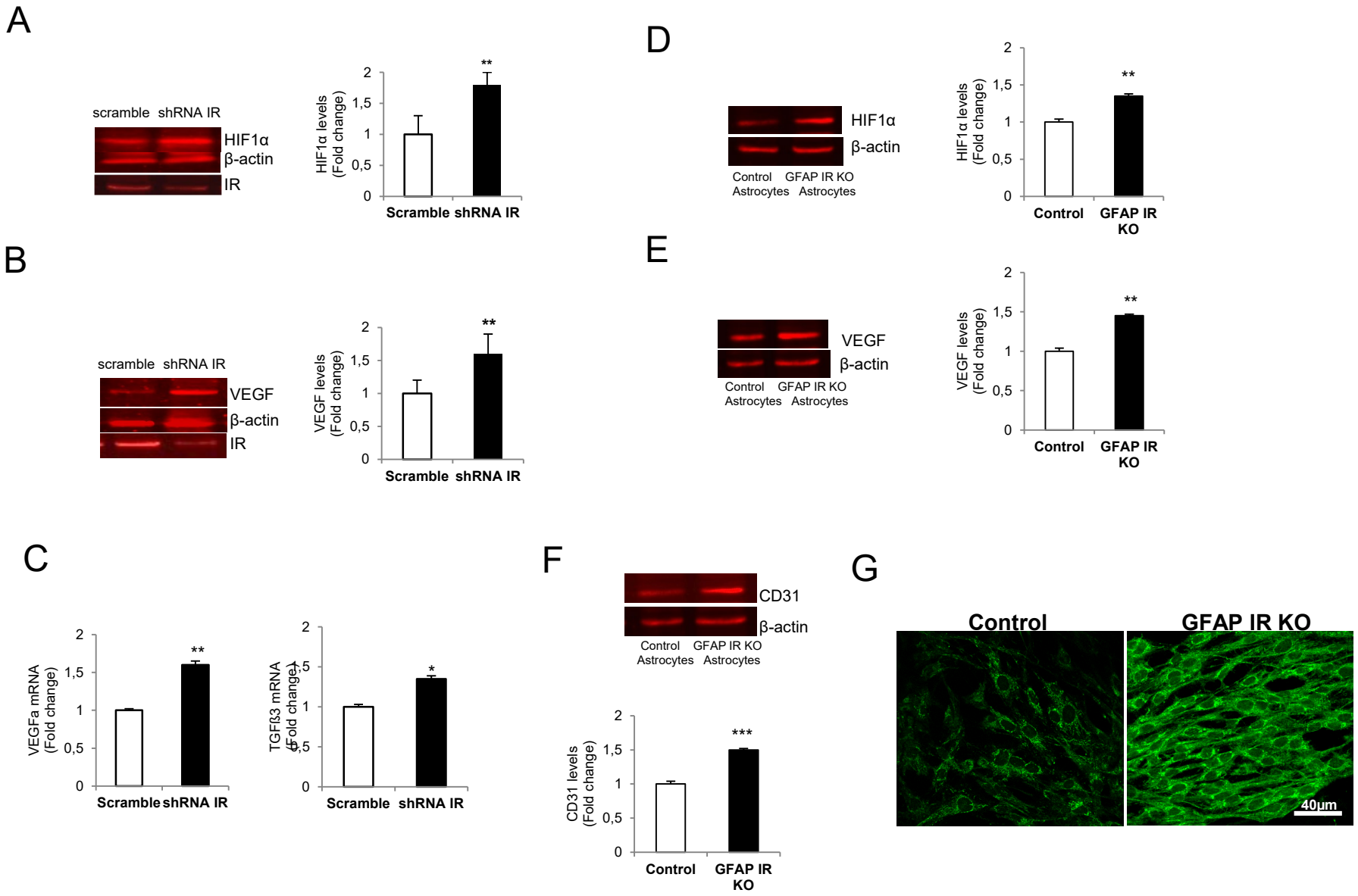
A
scramble shRNA IR
HIF1α
β-actin
IR
HIF1α levels (Fold change)
Scramble shRNA IR
B
scramble shRNA IR
VEGF
β-actin
IR
VEGF levels (Fold change)
Scramble shRNA IR
C
VEGFa mRNA (Fold change)
Scramble shRNA IR
TGFß3 mRNA (Fold change)
Scramble shRNA IR
D
HIF1α
β-actin
Control Astrocytes
GFAP IR KO Astrocytes
HIF1α levels (Fold change)
Control
GFAP IR KO
E
VEGF
β-actin
Control Astrocytes
GFAP IR KO Astrocytes
VEGF levels (Fold change)
Control
GFAP IR KO
F
CD31
β-actin
Control Astrocytes
GFAP IR KO Astrocytes
CD31 levels (Fold change)
Control
GFAP IR KO
G
Control
GFAP IR KO
40µm

Figure 8

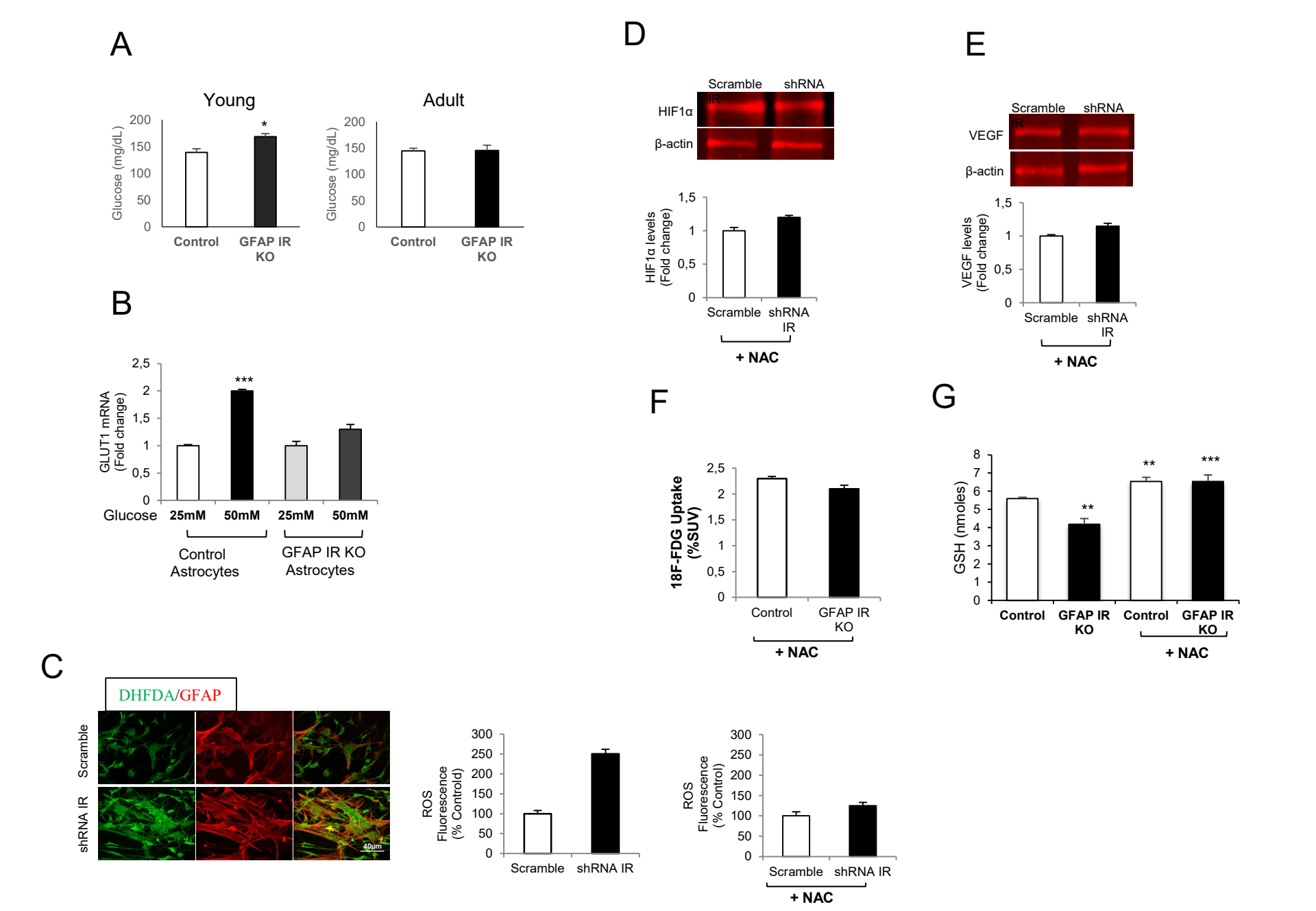
A
Young
Adult
Glucose (mg/dL)
200
150
100
50
0
*
Control
GFAP IR KO
B
GLUT1 mRNA (Fold change)
2,5
2
1,5
1
0,5
0
***
Glucose
25mM
50mM
25mM
50mM
Control Astrocytes
GFAP IR KO Astrocytes
C
DHFDA/GFAP
Scramble
shRNA IR
40µm
ROS Fluorescence (% Controld)
300
250
200
150
100
50
0
Scramble
shRNA IR
ROS Fluorescence (% Control)
+ NAC
D
Scramble
shRNA IR
HIF1α
β-actin
HIF1α levels (Fold change)
1,5
1
0,5
0
+ NAC
E
VEGF
β-actin
VEGF levels (Fold change)
+ NAC
F
18F-FDG Uptake (%SUV)
2,5
2
1,5
1
0,5
0
Control
GFAP IR KO
+ NAC
G
GSH (nmoles)
8
7
6
5
4
3
2
1
0
**
***
Control
GFAP IR KO
+ NAC

Figure 9

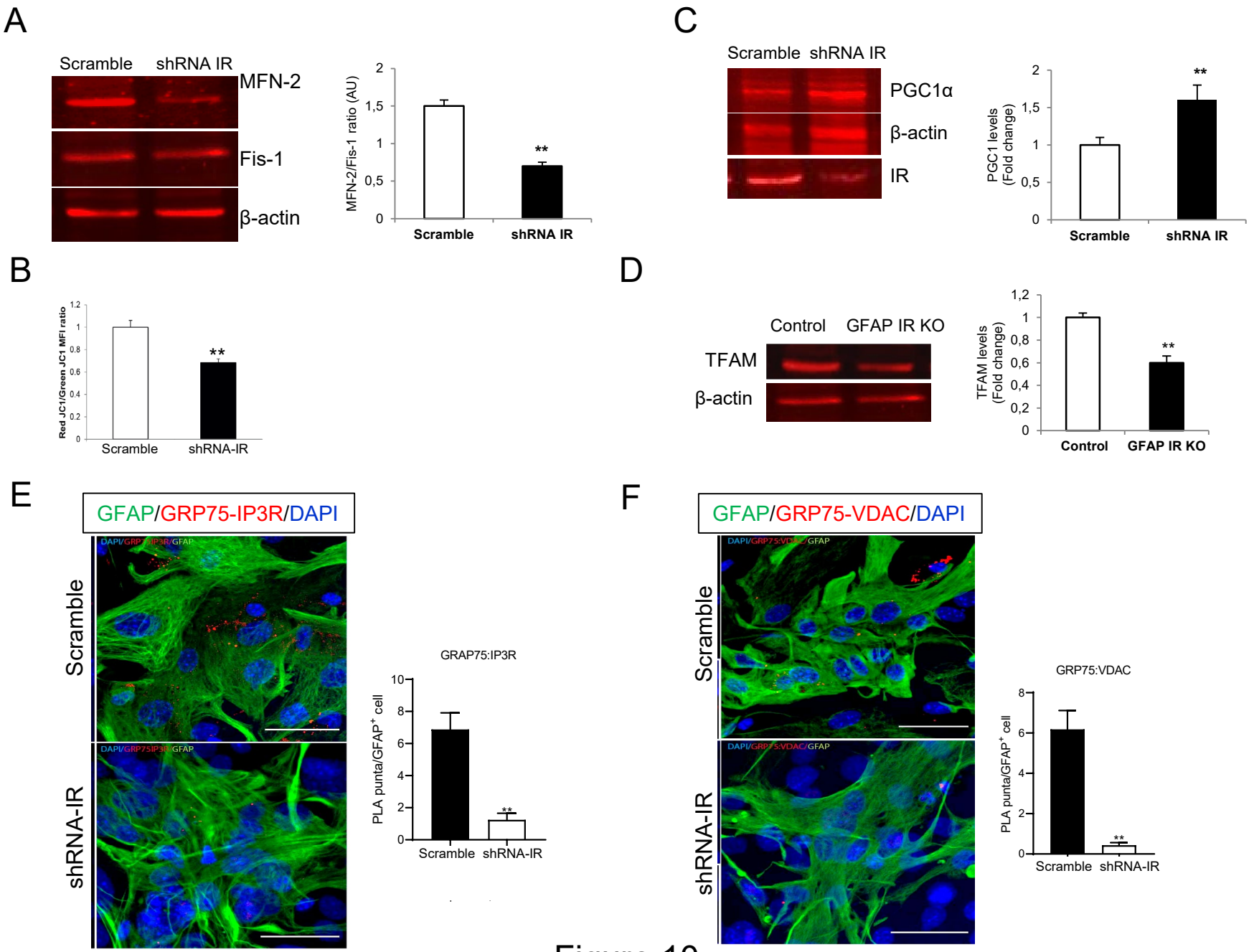
A
Scramble
shRNA IR
MFN-2
Fis-1
β-actin
MFN-2/Fis-1 ratio (AU)
Scramble
shRNA IR
B
Red JC1/Green JC1 MFI ratio
Scramble
shRNA-IR
C
Scramble
shRNA IR
PGC1α
β-actin
IR
PGC1 levels (Fold change)
Scramble
shRNA IR
D
Control
GFAP IR KO
TFAM
β-actin
TFAM levels (Fold change)
Control
GFAP IR KO
E
GFAP/GRP75-IP3R/DAPI
Scramble
shRNA-IR
GRAP75:IP3R
PLA punta/GFAP+ cell
Scramble
shRNA-IR
F
GFAP/GRP75-VDAC/DAPI
Scramble
shRNA-IR
GRP75:VDAC
PLA punta/GFAP+ cell
Scramble
shRNA-IR

Figure 10

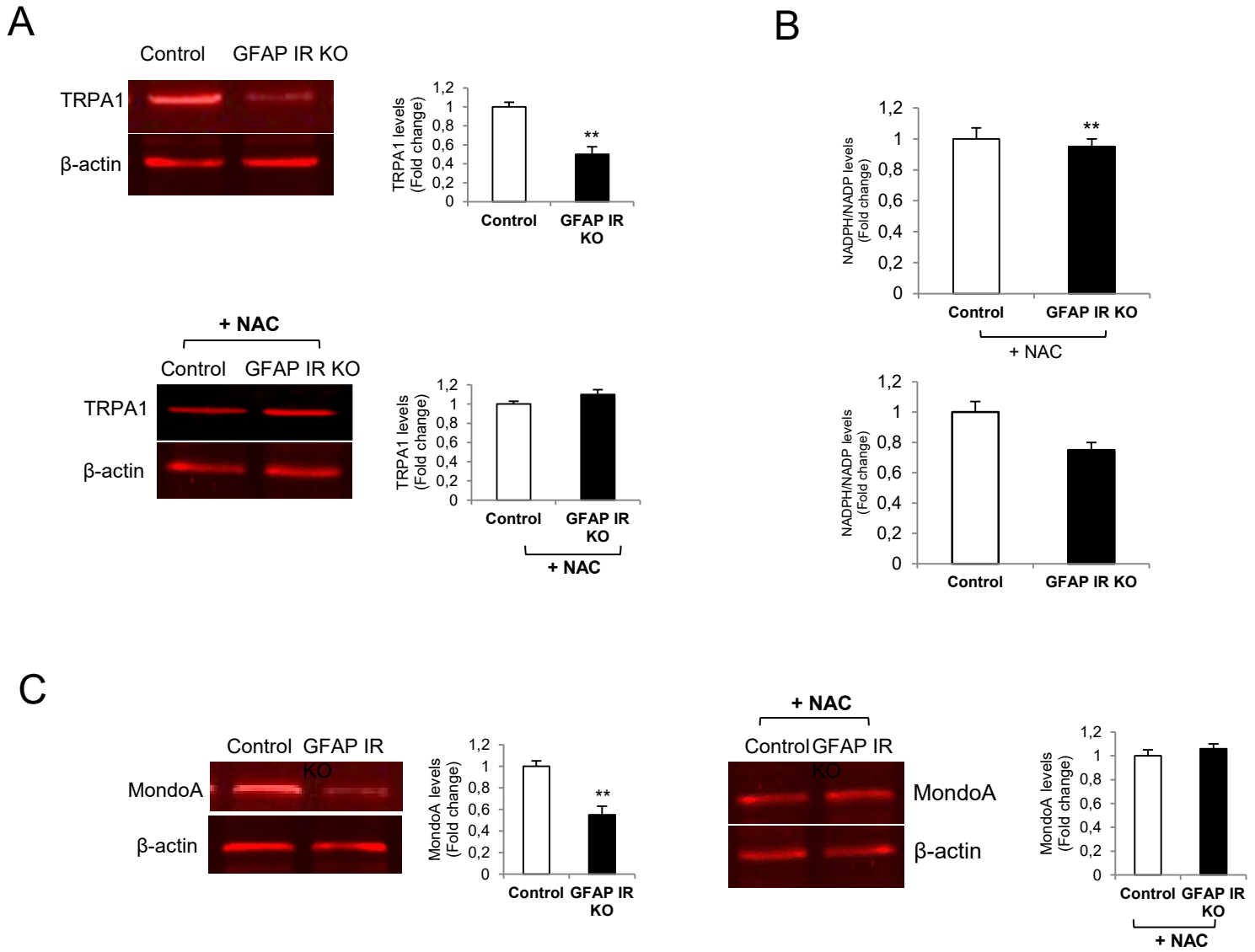
A
Control
GFAP IR KO
TRPA1
β-actin
TRPA1 levels (Fold change)
1,2
1
0,8
0,6
0,4
0,2
0
**
Control
GFAP IR KO
+ NAC
Control
GFAP IR KO
TRPA1
β-actin
TRPA1 levels (Fold change)
Control
GFAP IR KO
+ NAC
B
NADPH/NADP levels (Fold change)
1,2
1
0,8
0,6
0,4
0,2
0
**
Control
GFAP IR KO
+ NAC
NADPH/NADP levels (Fold change)
Control
GFAP IR KO
C
Control
GFAP IR KO
MondoA
β-actin
MondoA levels (Fold change)
**
Control
GFAP IR KO
+ NAC
Control
GFAP IR KO
MondoA
β-actin
MondoA levels (Fold change)
Control
GFAP IR KO
+ NAC

Figure 11

A

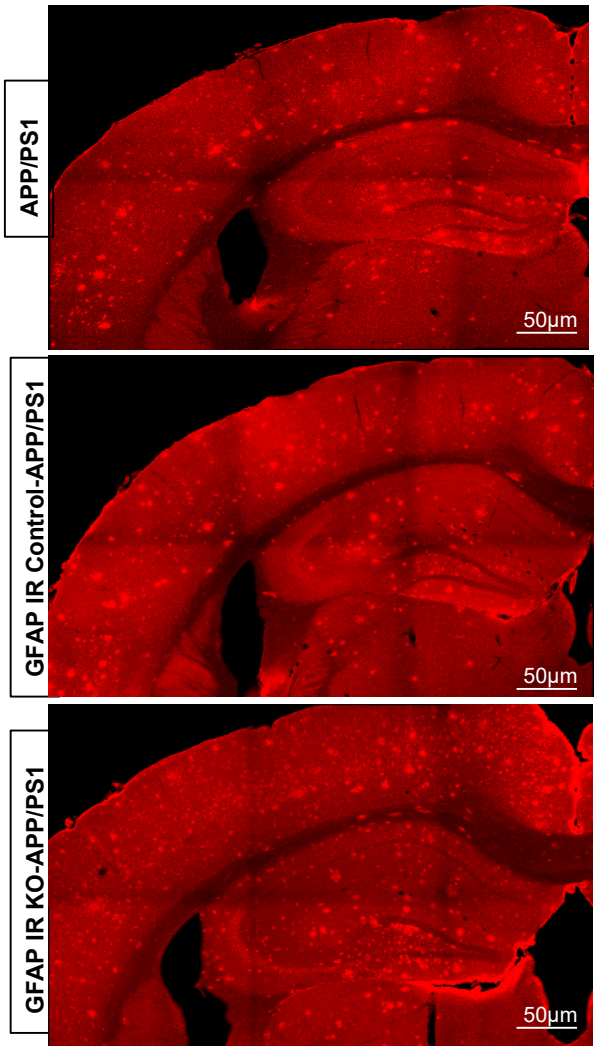
APP/PS1
50µm
GFAP IR Control-APP/PS1
50µm
GFAP IR KO-APP/PS1
50µm

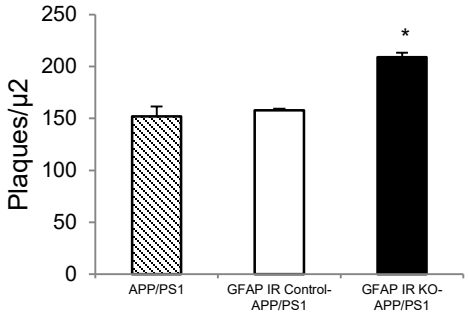
Plaques/µ2
250
200
150
100
50
0
*
APP/PS1
GFAP IR Control-APP/PS1
GFAP IR KO-APP/PS1

B

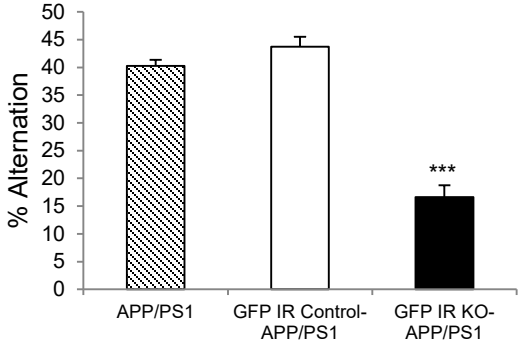
% Alternation
50
45
40
35
30
25
20
15
10
5
0
***
APP/PS1
GFP IR Control-APP/PS1
GFP IR KO-APP/PS1

Figure 12

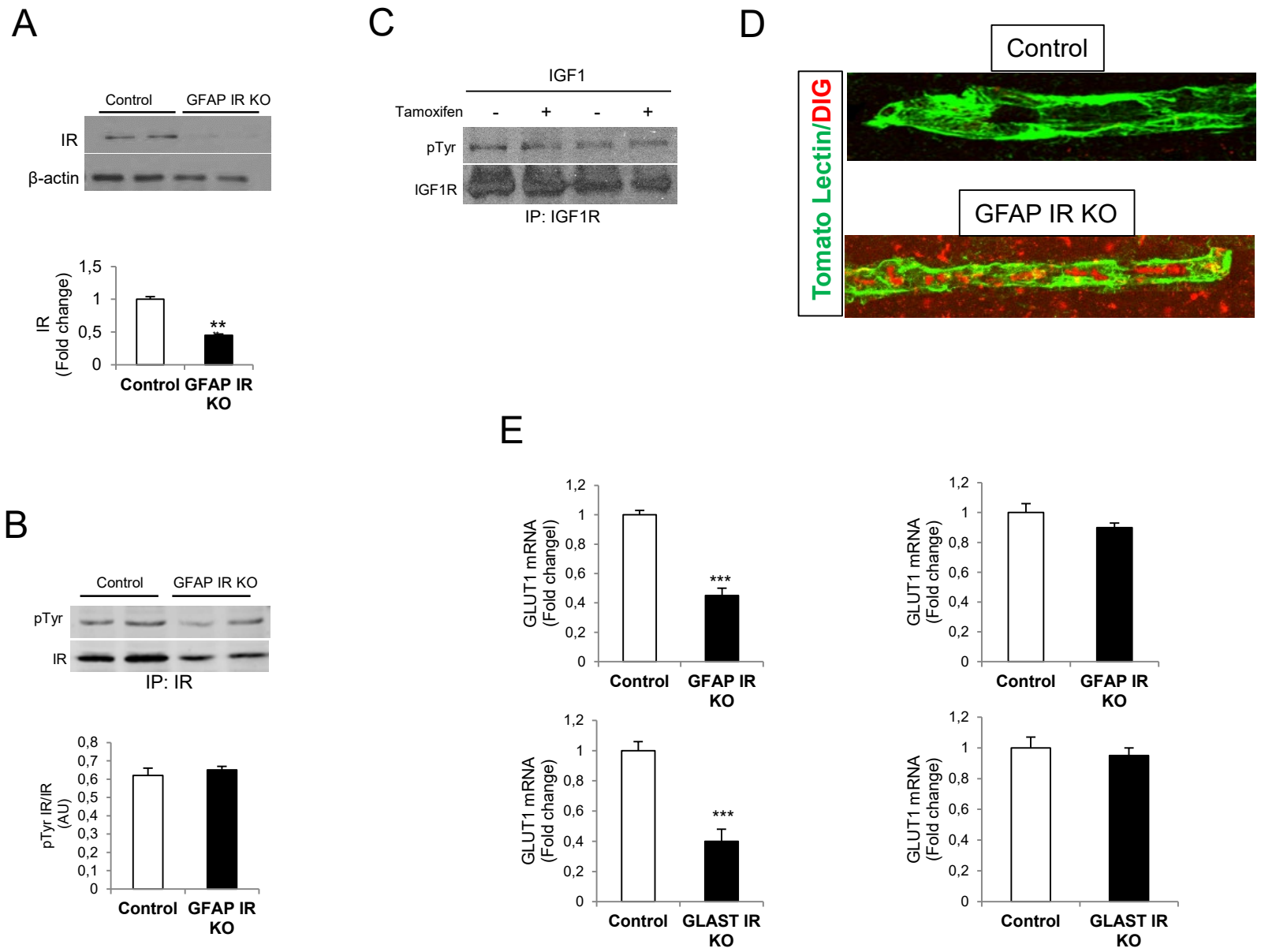

Supplementary Figure 1

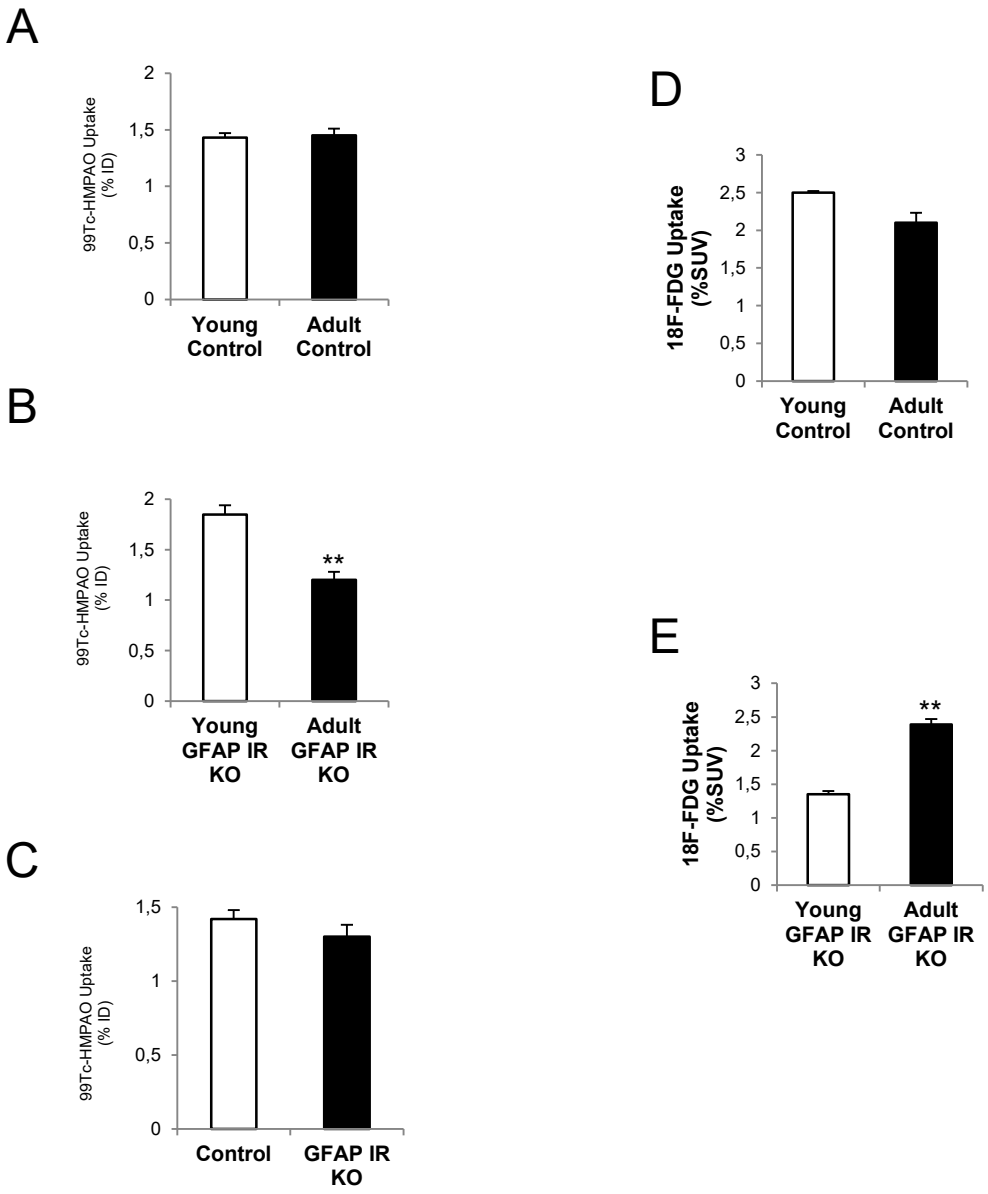

Supplementary Figure 2

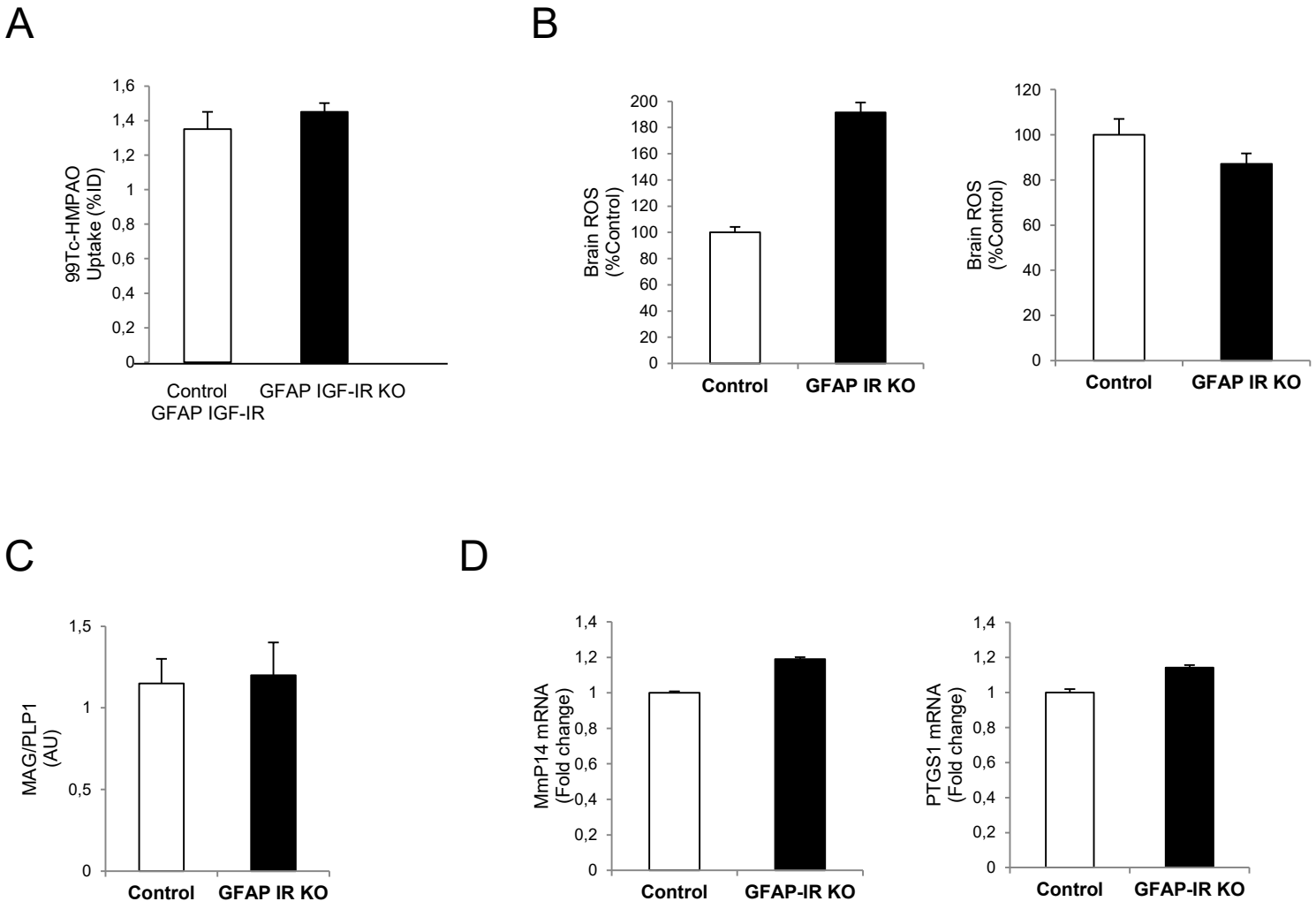

Supplementary Figure 3

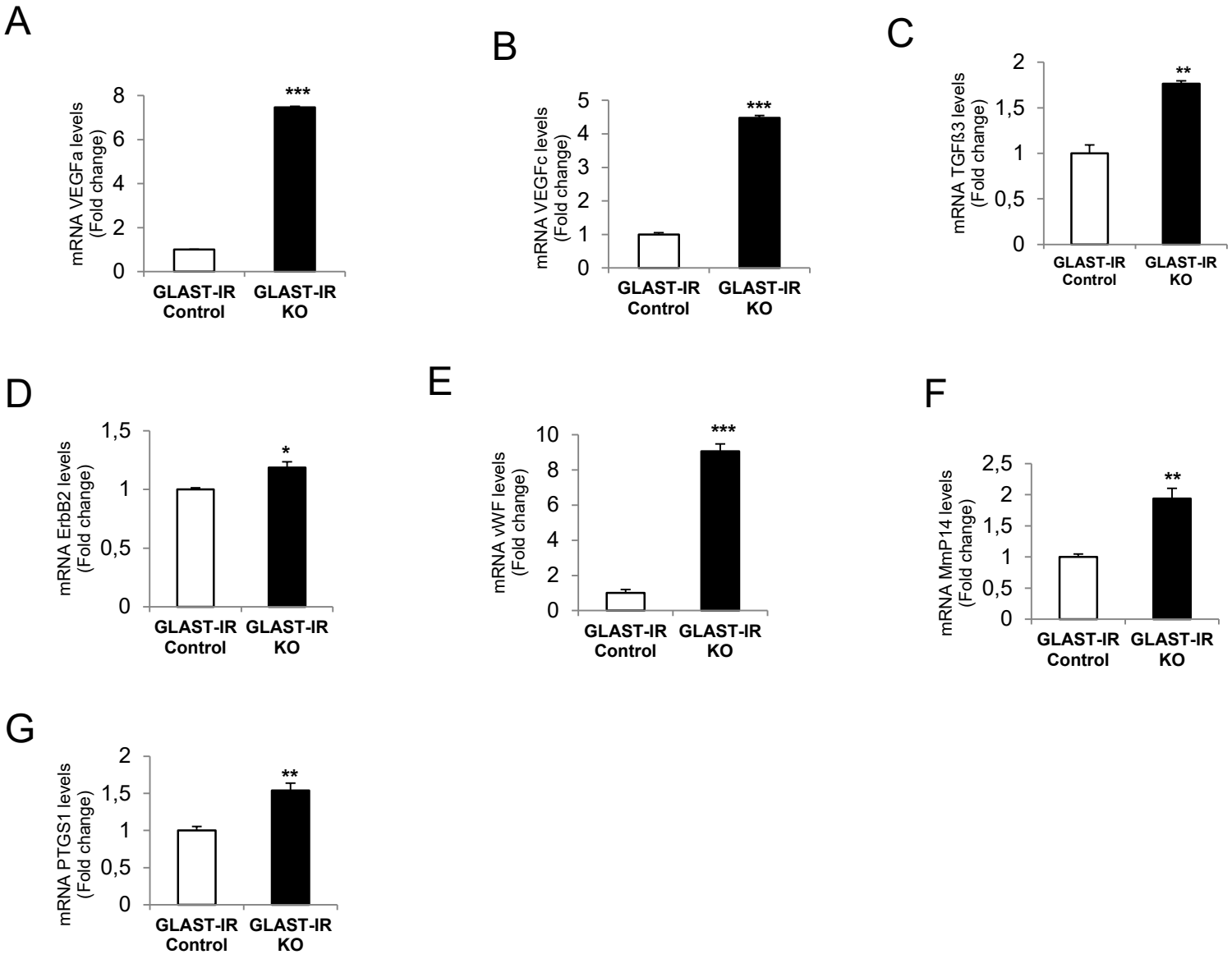

Supplementary Figure 4

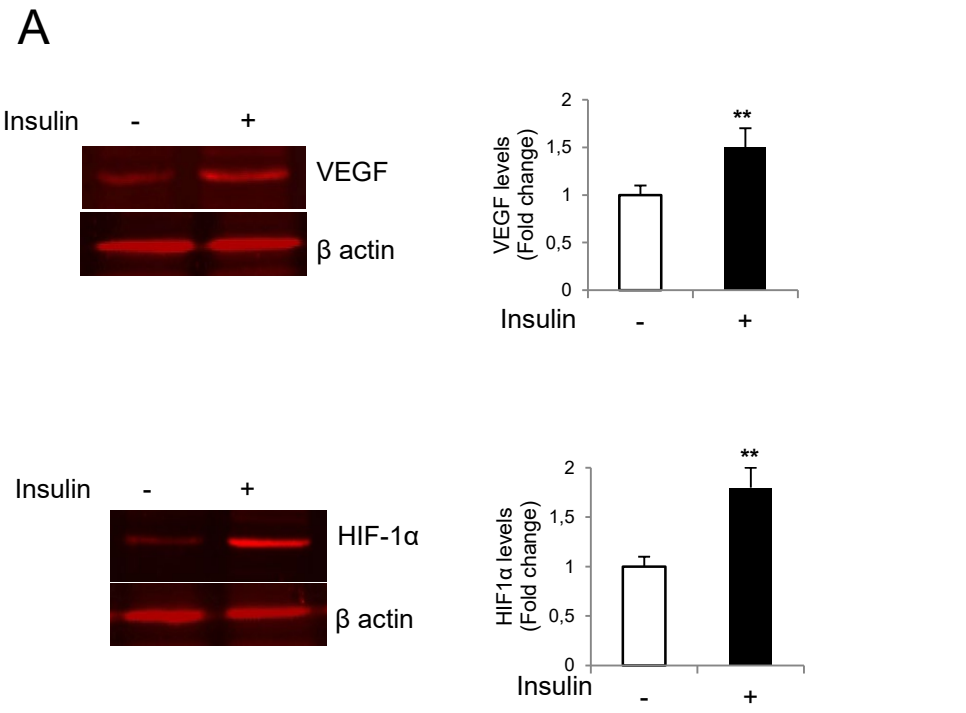

Supplementary Figure 5

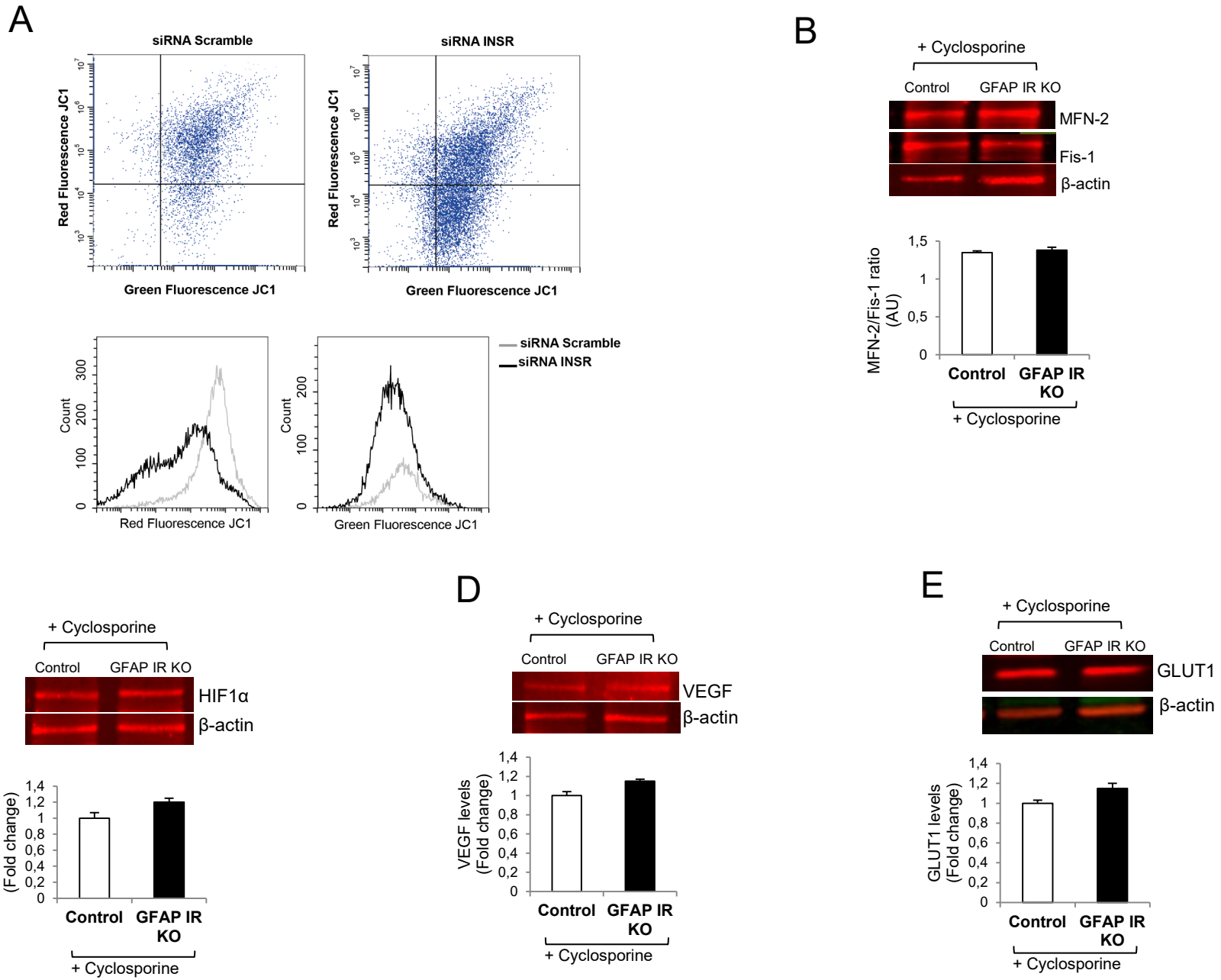

Supplementary Figure 6

A

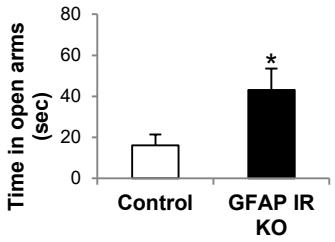

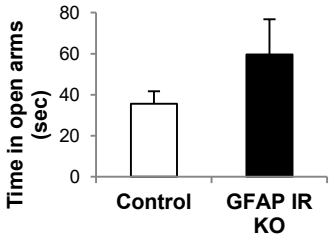

D

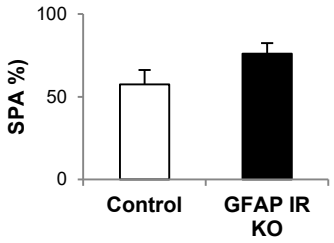

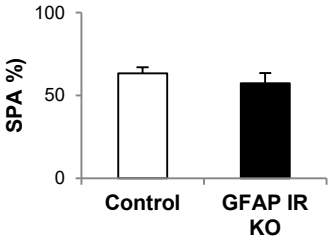

B

Modificar

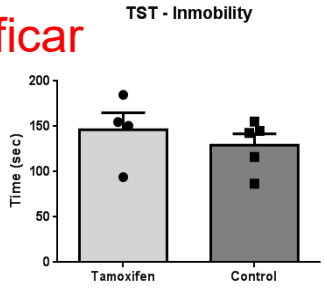

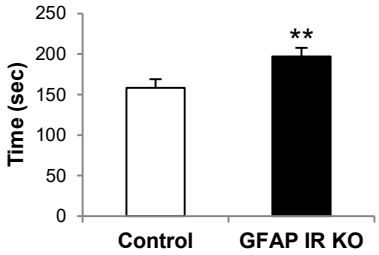

E

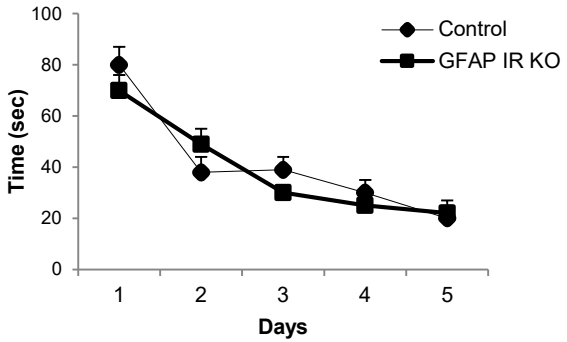

C

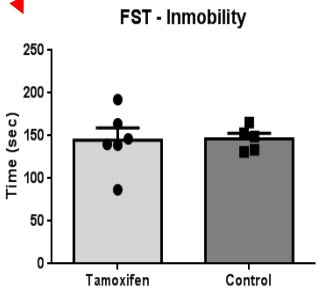

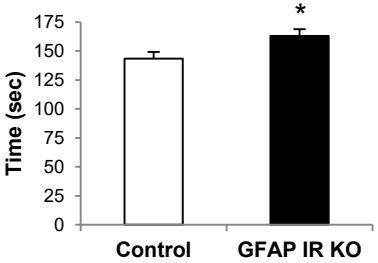

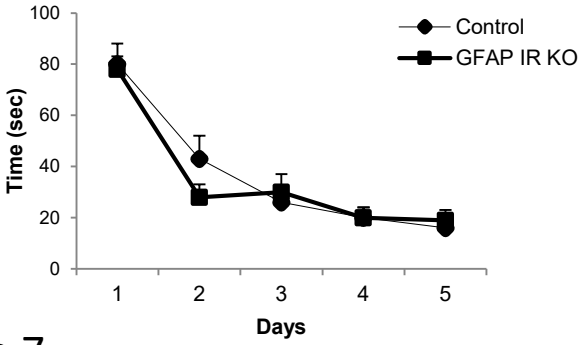

Supplementary Figure 7